UNIVERSITAT ROVIRA I VIRGILI

DEEEA
Departament d'Enginyeria Electrònica, Elèctrica i Automàtica

GRADUATED STUDENT MEETING

on

ELECTRONIC ENGINEERING

Tarragona, July 1, 2011

IEEE

Abstracts Book

Graduated Student Meeting

on

Electronic Engineering

Tarragona, July 1, 2011

Organising Comitee

Lluis F. Marsal

Josep Ferré-Borrull

Xavier Vilanova

Benjamí Iñiguez

Eduard Llobet

Angel Cid

Jordi Maré

Programme

Friday, 1st July

8:45 Opening Session
9:00 Plenary Session 1
Corinne Alonso
9:45 Plenary Session 2
Joachim N. Burghartz
10:30 Coffee break
11:00 Plenary Session 3
Stephan Roche
11:45 Plenary Session 4
Francesca Brunetti
13:00 Lunch
14:00 Poster Session
15:00 Plenary Session 5
Enric Garcia-Caurel
15:45 Plenary Session 6
Giovanni Pennelli
16:30 Poster Session and Coffee Break
17:30 Closing Session

Invited Speakers

Plenary Session 1

The smart-grid : what different possibilities of new research fields.

Corinne Alonso

Laboratoire d'Arquitecture et d'Analyse des Systèmes
Université de Toulouse-CNRS
France

Plenary Session 2

Ultrathin chips: a paradigm shift in silicon technology

Joachim N. Burghartz

IEEE EDS Distinguished Lecturer
IMS-Chips
Stuttgart, Germany

Plenary Session 3

Exploring Quantum Transport in Graphene-based Devices: From Novel Device Principles to Spintronics

Stephan Roche

Institut Català de Nanotecnologia
Bellaterra, Spain

Plenary Session 4

Introduction to polymer solar cells

Francesca Brunetti

Universitá di Roma 2
Italy

Plenary Session 5

Optical Characterization of Semiconductors Using Polarized Light

Enric Garcia-Caurel

Laboratoire de Physique des Interfaces et des Couches Minces
École Polytechnique-CNRS
France

Plenary Session 6

Silicon nanowires: building blocks for advanced electronic devices

Giovanni Pennelli

Facoltà di Ingegneria
Universita degli Studi di Pisa
Italy

Index

Invited Speakers

Posters

Plenary Sessions

The smart-grid : what different possibilities of new research fields.

Corinne Alonso

Laboratoire d'Arquitecture et d'Analyse des Systèmes
Université de Toulouse-CNRS
France

The fossil energies present in the future (less than 20 years) high limits in supplies because their limited ressources. Renewable energies can be a part of alternative solutions but present technical limits in particular linked to their intermittent nature.

The smart-grid concept first developped in the sixties in USA represents now a global challenge for the power distribution companies but also ICT ones like google. The complexity of a grid needed new technological developpments in several parts of control, sensor, data and energy storage, energy sources and their optimised management but also certainly a radical change of stylelife.

A vision by PV source is developped to illustrate purposes.

Ultrathin chips: a paradigm shift in silicon technology

Joachim N. Burghartz

IEEE EDS Distinguished Lecturer
IMS-Chips
Stuttgart, Germany

Silicon not only features the known good electronic properties but is also an excellent mechanical material. While in microelectronics the mechanical properties of silicon are of little importance micro electromechanical systems (MEMS) have taken advantage of them. In contrast to conventional microelectronics and MEMS ultra- thin chip technology exploits both the electronic and micro mechanical capabilities of silicon. Therefore, ultra-thin chips drive entirely new applications, such as 3D integrated circuits (3D-ICs) and systems-in-foil (SiF), and feature a paradigm shift in silicon technology. This talk will introduce and compare the generically different process technologies that can be exploited for the fabrication of ICs on extremely thin chips. Furthermore, several applications with the associated engineering issues will be presented and discussed based on material that has been presented at IEDM and ISSCC conferences in recent years.

Brief Biography:

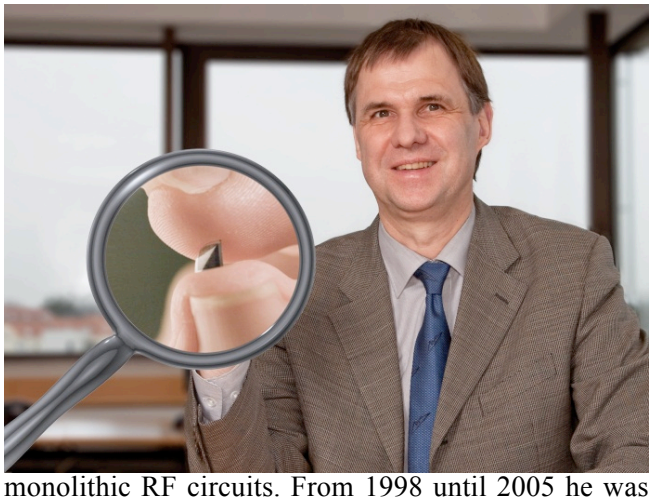

Joachim N. Burghartz is an IEEE Fellow, an IEEE Distinguished Lecturer, and an ExCom member of the IEEE Electron Devices Society. He received his MS degree from RWTH Aachen in 1982 and his PhD degree in 1987 from the University of Stuttgart, both in Germany. From 1987 thru 1998 he was with the IBM T. J. Watson Research Center in Yorktown Heights, New York, where he was engaged in early development of SiGe HBT technology and later in research on integrated passive components, particularly inductors, for application to monolithic RF circuits. From 1998 until 2005 he was with TU Delft in the Netherlands as a full professor and from 2001 as the Scientific Director of the Delft research institute DIMES. In fall 2005 he moved to Stuttgart, Germany, to head the Institute for Microelectronics Stuttgart (IMS CHIPS). In addition he is affiliated with the University of Stuttgart as a full professor. Dr. Burghartz has published about 300 reviewed articles and holds more than 30 patents.

Exploring Quantum Transport in Graphene-based Devices: From Novel Device Principles to Spintronics

Stephan Roche

Catalan Institute of Nanotechnology (ICN)-CIN2
Theoretical & Computational Nanoscience Group
Email: stephan.roche@icn.cat

This talk will focus on the presentation of new type of device principles unique to graphene-based-materials, driven by chemical doping, functionalization, mechanical stress or patterning (superlattices). To circumvent the current hurdles preventing the advent of graphene nanoelectronics, it has become urgent to benefit from engineering complexity at the nanoscale an the unique potential of graphene as a bridging platform between top-down conventional CMOS technologies and (bio)-chemistry self-assembling processes.
Here, by using state-of-the-art multiscale simulations (combining first-principles with tight-binding schemes), we present several electronic transport features in complex forms of chemically modified graphene based materials. This includes the use of boron or nitrogen-doped to produce graphene-based nanoribbons exhibiting "mobility gaps" of width as large as 1eV, providing an efficient switching behavior principle even in the presence of a vanishing electronic band-gap. The possibility to design a switching effect based on mechanical deformation of graphene nanoribbons. Finally, the future for graphene-based spintronics will be discussed. The possibility for intrinsic spin polarized states (ribbon edge states), or defect-driven intrinsic magnetic ordering will be presented from a theoretical perspective and in comparison with most recent experiments.

Related bibliography

D. Soriano, N. Leconte, P Ordejon, J.-Ch. Charlier, J.-J. Palacios, and **S. Roche**
Magnetoresistance and Magnetic Ordering Fingerprints in Hydrogenated Graphene
Phys. Rev. Lett. (in press)
N. Leconte, D. Soriano, **S. Roche**, P. Ordejon, J.-Ch. Charlier, and J. J. Palacios
Magnetism-Dependent Transport Phenomena in Hydrogenated Graphene: From Spin-Splitting to Localization Effects
ACS Nano 5, 3987 (2011); DOI: 10.1021/nn200558d
B. Biel, F. Triozon, X. Blase, and **S. Roche**,
Chemically-induced Mobility Gaps in Graphene Nanoribbons: A Route to Improve Device Performances
Nano Lett. 9, 2725 (2009)
E. Erdogan, I. Popov, C. G. Rocha, G. Cuniberti, **S. Roche** and G. Seifert,
Engineering carbon chains from mechanically stretched graphene-based materials
Phys. Rev. B 83, 041401 (Rapid Communication) (2010).

Introduction to polymer solar cells

Fancesca Brunetti

Universitá di Roma 2
Italy

Polymer solar cells represent a promising technology for the mass low-cost and large-area production of organic solar cells, suitable also for flexible substrates.
In this lecture an introduction to the working principle of polymeric solar cells will be given. The realization methodologies, namely single layer, multilayer and bulk-heterojunction will be analyzed evidencing the advantages and disadvantages of each approach. Different devices and architectures will be discussed.
Furthermore, the key role of the morphological control on the device performance will be analyzed as a function of the realization process (role of solvent and annealing conditions).
An overview of the technologies used and their application on large area production will be presented.

Optical Characterization of Semiconductors Using Polarized Light

E.Garcia-Caurel, R.Ossikovski, A. de Martino
Laboratoire de Physique des Interfaces et des Couches Minces
École Polytechnique-CNRS
91128, Palaiseau, France

1. Introduction

The use of light in material science as tool for characterization has several advantages such as the non-invasiveness, and the easiness of use. All optical techniques have in common the measurement of the intensity of light, but some of them go a step further and take profit of polarization as an additional source of information. The goal of this presentation is to present briefly several techniques such as spectroscopic ellipsometry, polarimetry and near-field polarization Raman spectroscopy, which have potential applications for nano-electronics.

2. Ellipsometry

Ellipsometry is a very sensitive and widespread characterization technique based on the measurement of light polarization changes due to the interaction (reflection, transmission or scattering) of the probe light beam with the sample under study [1]. Ellipsometry provides complete characterization of the sample only in specific cases, such the usual configuration involving isotropic surfaces as schematized in fig. 1.

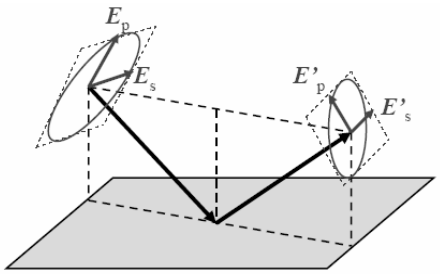

Fig.1: Typical ellipsometric characterization of isotropic surfaces.

Many mature ellipsometric techniques and commercial apparatus are available [2, 3]. Spectroscopic ellipsometry is by far the most widespread modality, as it is particularly well suited to the characterization of materials via their spectrally resolved dielectric functions, and thin film stacks, which produce spectral fringes related to layer thicknesses and dielectric functions. Ellipsometry can also be implemented with angular resolution [4], or in imaging modes [5]. In this latter case, extremely small thickness differences can be monitored from one site to another, for example for "lab-on-a-chip" applications.

3. Mueller polarimetry

Classical ellipsometry cannot provide reliable information when anisotropy, or depolarization due to inhomogeniety are present. For such cases there exists a more general approach called Mueller polarimetry [6]. This generalization has a cost one needs to perform at least 16 measurements instead of 2 for classical ellipsometry. The recent availability of reliable and easy to use liquid crystal retarders have made possible the development of a wide variety of Mueller polarimeters. The first one was a spectroscopic version working in the visible that now is commercially available under the name of MM16.[7]. A more recent set-up, shown in figure 2, consists of an angular-resolved polarimeter imager with a high spatial resolution (diffraction limited) of 50µm [8]. Both apparatus have been used to the analysis of nanostructures such as 1D and 2D diffraction gratings. The experimental data was fitted to parametric models describing the profile of the gratings and it has been found that the profile could be reconstructed with a precision of a few nm (figure 2).

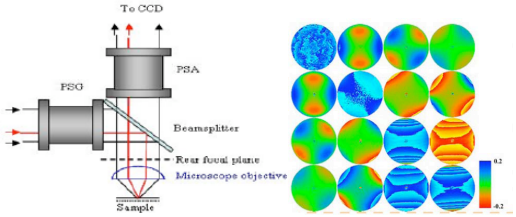

Fig.2: Schematic representation of the angle resolved Mueller polarimeter (left). Angle resolved Mueller matrix of a 1D diffraction grating.

The coupling of a diffraction grating to a solar cell may enhance the light trapping and hence the overall conversion efficiency of the cell. The use of both, spectroscopic and angle-resolved Mueller polarimeters, to characterize the nanostructured cell and correlate optical properties with structural properties of the grating is a promising field of applications.

4. Near-field polarized Raman spectroscopy

Raman microscopes take full advantage of diffraction-limited optics to provide molecular and crystalline information on a size scale of the order of the laser wavelength [9]. Going beyond the diffraction limit can only be achieved by

implementing some special technique like near-field optics. Near-field Raman scanning microscopy has been developed by delivering and/or collecting light with a tapered optical fiber [10]. However, to avoid the important optical losses caused by the fiber, a new technique has been developed. This technique takes advantage of nanoscale manipulations of an Atomic Force Microscope (AFM) and the Surface Enhanced Raman Scattering Effect (SERS). SERS is a phenomenon in which material in intimate contact with particles of noble metals (Ag, Au or Cu) experiences an enhancement of its Raman cross-section by 6 to 14 orders of magnitude. To integrate AFM with SERS, the tip is coated with one of the SERS enhancing metals. The AFM tip is scanned in the proximity to the sample surface and it produces a "local SERS". This technique is called Tip Enhanced Raman Spectroscopy (TERS). The spatial resolution is determined by the TERS signal across the sample, and is approximated by the dimension of the tip. Several academic groups have shown TERS setups in both, transmission and reflection geometries.

Polarization sensitive TERS can be realized by polarizing the incident beam with a linear polarizer and analyzing the state of polarization of the scattered light by a second polarizer placed just before the detector. In the case of crystalline silicon it is possible to design a measurement that minimizes the far field Raman signal (by controlling the orientation of the crystal's axes relative to the laser and Raman polarization) while still "allowing" the TERS signal[11]. By taking advantage of the TERS system, image resolution is about 100nm. Figure 3 show normal Raman maps of a GaN nanowire.

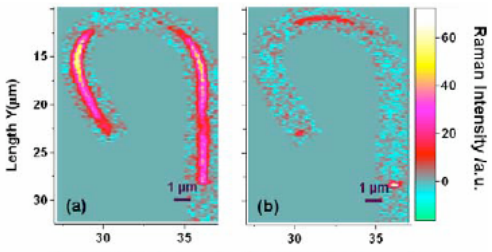

Fig.3: Near-field Raman image of GaN Nanowire. The maps correspespond to different polarization conditions.

Polarized Raman Spectroscopy in oblique incidence has also been applied to fully determine the stress tensor of silicon films of different thickness deposited on SiGe subtrates [12]. This has been possible because phonon modes are selectively modified when the material is submitted to a mechanical stress. A methodology relating the stress-induced frequency shifts and line-widths of the phonon absorption peak to the stress tensor components within the adopted experimental configuration was developed. The method consists of monitoring the variations of the stress-sensitive peak frequencies and line-widths while rotating stepwise the sample about its normal. Figure 4 shows the variations of the peak position for one of the samples analyzed.

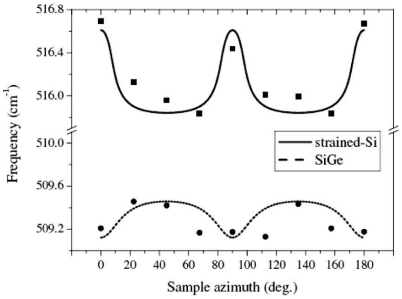

Fig.4: Measured (points) and fitted (lines) effective peak frequencies of the Si–Si phonon vibration from strained Si lattices vs the sample azimuth

Acknowledgements

Participation to SiNEP-09 meeting has been supported by the European project NANOCHARM.

References

[1] R.M.A. Azzam, N.M. Bashara, Ellipsometry and polarized Light (Nord Holland, 1989).
[2] P.S. Hauge, Surf. Sci., vol.96, pp.108 (1980)
[3] D.E. Aspnes, Thin Solid Films, vol.455, pp.828 (2004).
[4] H.-T. Huang, F.L. Terry, Jr., Thin Solid Films vol.455 pp.828 (2004).
[5] M. Vaupel, S. Yunfeng, Y. Zhimin, phys. stat. sol. (a) vol.205, pp.772 (2008).
[6] R.A. Chipman, Handbook of Optics, vol. 2, (McGraw Hill), (1995).
[7] E.Garcia-Caurel, A. De Martino, B. Drévillon, Thin Solid Films, vol.455, pp.120 (2004)
[8] S. Ben Hatit, M. Foldyna, A. De Martino, B. Drévillon, Phys. Stat. Sol (a), vol.205, pp.743 (2008)
[9] M Delhaye; P Dhamelincourt; J Raman Spectrosc., vol.3; pp.33 (1975)
[10] E. Betzig, J.K. Trautman, T.D. Harris, J.S. Weiner, R.L. Kostelak Science, vol.251, pp.1468 (1991).
[11] D. Mehtani, N. Lee, R.D. Hartschuh, A. Kisliuk, M.D. Foster, A. P. Sokolov, and J. F. Maguire, J. Raman Spectrosc., vol. 36, p.1068 (2005)
[12] R. Ossikovski, Q. Nguyen, G. Picardi, J. Schreiber, J. Appl. Phys., 103, 093525 (2008)

Silicon nanowires: building blocks for advanced electronic devices

Giovanni Pennelli
Facoltà di Ingegneria
Universita degli Studi di Pisa
Italy

Nowadays there are great investments for the development of advanced silicon nanostructures. Between them, silicon nanowires (SiNWs) are largely investigated with the aim of fabricating advanced devices for applications in several fields as nanoelectronics, nanophotonic, photovoltaic conversion, nanosensors and nanoelectromechanical systems.
A quite new and very promising field is the employment of SiNWs for the realization of high efficiency thermoelectric devices, for intriguing applications in energy harvesting.
Devices based on SiNW can be fabricated essentially by two approaches: nanoscale structures, obtained by several chemical deposition techniques, can be assembled with contacts and control gates in the bottom up approach. Conversely, the top down approach starts from a substrate and uses high resolution lithography, etchings, film depositions and other processes for the fabrication of nanometric structures. With this approach, SiNWs can be fabricated already aligned to contacts and control gates, in such a way that complex devices can be easily produced. Both approaches have positive and negative aspects, but probably the top down one is more compatible with standard CMOS processing.
A top down process, based on electron beam lithography, silicon anisotropic etching and stress controlled oxidation will be presented, and devices based on silicon nanowires smaller than 10 nm in diameter, and several micrometers long, will be shown.

Posters

Optical characterization of nanoporous anodic alumina formed in oxalic acid solution

M. Alba, A. Santos, P. Formentín, J. Ferré-Borrull, J. Pallarés and L. F. Marsal

Departament d'Enginyeria Electrònica, Elèctrica i Automàtica, ETSE, Universitat Rovira i Virgili, Avda. Països Catalans 26, 43007 Tarragona, Spain
lluis.marsal@urv.cat

Abstract

We report on the photoluminescence properties of nanoporous anodic alumina fabricated under mild and hard anodization conditions using oxalic acid as alectrolyte. It was observed that the anodization conditions, i.e. voltage applied, as well as the pore size make a noticeable variation in alumina photoluminescence properties in both intensity and peak position.

1. Introduction

Nanoporous anodic aluminum oxide (AAO) fabricated by electrochemical oxidation is a self-ordered nanopore material that has attracted for decades the interest of the scientific community [1-2]. The intrinsic properties of AAO such as optical transparency and temperature stability, coupled with the fact that widths and lengths of the pore can be tuned by adjusting the anodization conditions, make AAO unique nanometer-scale template. A wide range of structures such as fibrils, pillars, rods and wires with application in optoelectronics, micro-electronics or solar cells have been lately developed using AAO as a template [2-5]. However, the properties of AAO itself affect the properties of the materials based on the AAO, which makes necessary a full optical characterization.

Herein, we report the optical properties of nanoporous alumina fabricated by mild and hard anodization in oxalic acid and subsequently subjected to an etch treatment. The AAO samples were microscopically characterized by ESEM. Optical properties were studied by measuring the PL, reflectance and transmittance.

2. Experimental results

Nanoporous AAO was prepared by electrochemical etching of high purity aluminum foil. Two different well-known methods were performed: mild anodization (MA) and hard anodization (HA). MA consists of two steps [1]. First anodization step was carried out at 40 V for 16 h in oxalic acid 0.3 M. Then the alumina layer was removed in a mixture of phosphoric acid (H_3PO_4) 0.4 M and chromic acid ($H_2Cr_2O_7$) 0.2 M for 3 h at 70ºC. After this, the aluminum foil was anodized again for 15 h under the same conditions. HA was also performed, following well-established procedures [5]. First 40 V for 10 min were applied to form a thin oxide layer. Subsequently, the anodization voltage was slowly increased to 140 V for HA at a rate of 0.1 V/s and the HA will be continued under this constant potential for 30 min. Final structures are high-ordered and 50 μm thick, for both MA and HA. The remaining aluminum substrate was removed by a $CuCl_2$/HCl solution to form AAO with exposed barrier layer. For HA alumina the oxide barrier layer was removed by wet chemical etching using a H_3PO_4 aqueous solution. Finally, pore widening treatment was performed in H_3PO_4 5 %wt to obtain different pore sizes in both MA and HA alumina. The morphology and pore size of the top and bottom surfaces of MA and HA samples, respectively, were characterized by ESEM (see Fig. 1(a-d) and Fig. 2(a-d)).

The PL spectra of the MA and HA a without etch treatment are shown in Fig. 3. Both samples show a broad PL band (350-550 nm), with very similar intensity and width. However it was observed a red shift (from 442 to 455 nm) in the PL emission when increasing the anodization voltage from 40 V to 140 V. The etch treatment, and consequently the pore diameter, was found to affect the PL intensity for both MA and HA samples. Fig. 4(a) and (b) show that the PL intensity and the pore diameter increase with the etching time. MA and HA alumina behave quite similar in response to the etching time and PL excitation, with no significant shift of peak position.

3. Conclusions

We have fabricated nanoporous alumina by anodization under mild and hard conditions and then wet chemically etched to obtained different pore sizes. The emission peak for HA alumina is located at longer wavelengths than MA alumina. The intensity of the PL spectra increased with the increase of the etching time, i.e. the increase of the pore diameter, for both MA and HA alumina.

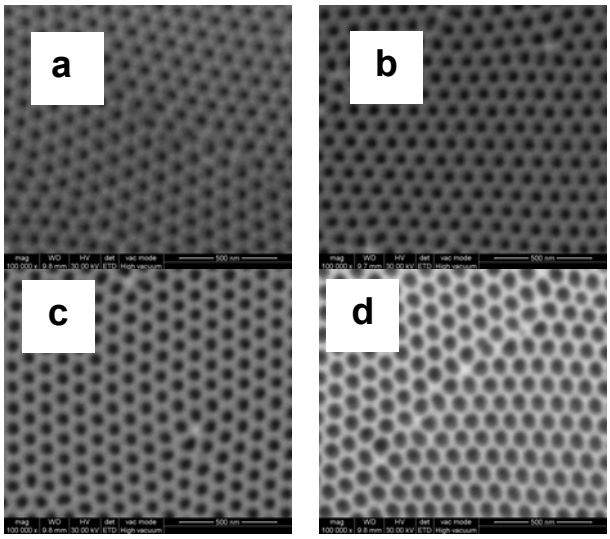

Fig.1. ESEM images of alumina samples prepared by mild anodization using oxalic acid and subjected to chemical etching for 0 min (a), 8 min (b) 16 min (c) and 24 min (d).

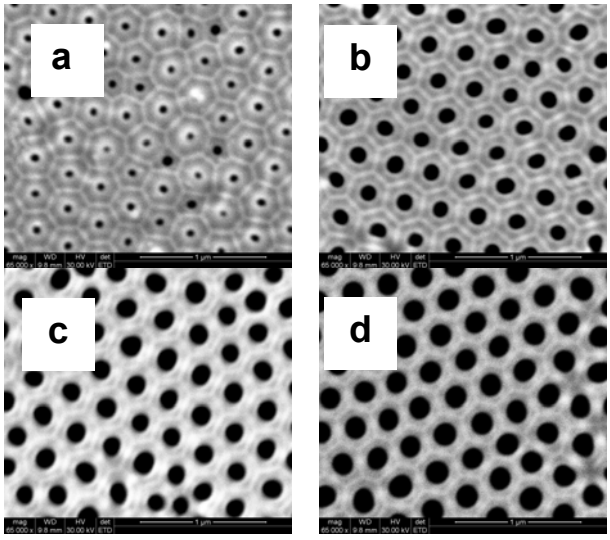

Fig.2. Fig.1. ESEM images of alumina samples prepared by hard anodization using oxalic acid and subjected to chemical etching for 0 min (a), 15 min (b) 30 min (c) and 45 min (d).

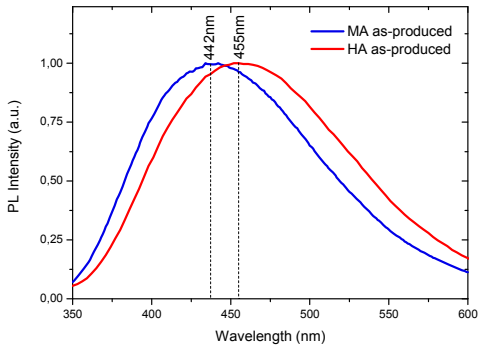

Fig.3 Normalised PL spectra for as-produced samples using MA and HA anodizations under 335 nm excitation.

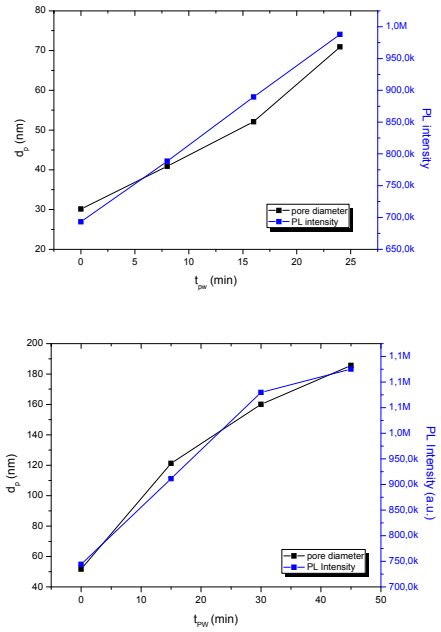

Fig.4. Dependence of the pore diameter and PL intensity upon etching time for MA (a) and HA (b) alumina.

Acknowledgments

This work was supported by Spanish Ministry of Ciencia e Innovacion (MICINN) under grant number TEC2009-09551, HOPE CSD2007-00007 (Consolider-Ingenio 2010) and by the Generalitat de Catalunya under project 2009SGR549.

.

References

[1] H. Masuda, K. Fukuda "Ordered metal nanohole arrays made by a 2-step replication of honeycomb structures of anodic alumina", *Science*, vol 268, pp 1466-1468, Jun 1995.

[2] G.E. Thompson "Porous anodic alumina: fabrication, characterization and applications", *Thin Solid Films*, vol 297(1-2), pp 192-201, May 1997.

[3] G. Che, B.B. Lakshmi, C.R. Martin, E.R. Fisher, R.S. Ruoff "Chemical vapor deposition based synthesis of carbon nanotubes and nanofibers using a template method", *Chemistry of material*, vol 10, pp 260-267, Jan 1998.

[4] D. Losic, J.G. Shapter, J.G. Mitchell, N.H. Voelcker, "Fabrication of gold nanorod arrays by templating from porous alumina", *Nanotechnology*, vol 16, pp 2275-2281, Jun 2005.

[5] N. Haberkorn, J.S. Gutman, P. Theato, "Template-assisted fabrication of free-standing nanorod arrays of a hole-conducting cross-linked triphenylamine derivative: toward ordered bulk-heterojunction solar cells", *ACS Nano,* vol 3, pp 1415-1422, May 2009.

[6] W. Lee, R. Ji, U. Gösele, K. Nielsch, "Fast fabrication of long-range ordered porous alumina membranas by hard anodization", *Nature,* vol 5, pp 741-747, Aug 2006.

Enhancing the sensing layer based on WO3 nanoneedles deposited by AACVD

F.E.Annanouch[1], E. Llobet

[1] DEEEA, Universitat Rovira i Virgili Tarragona, Spain

Fatima Ezahra Annanouch, Departament d'Enginyeria Electrònica, Elèctrica i Automàtica, Universitat Rovira i Virgili

Avinguda dels Països Catalans, 26 Campus Sescelades, 43007 TARRAGONA (Spain)

Tel. +34 977 256 572, e-mail: fatimaezahra.annanouch@urv.cat

Abstract

Sensing layers based on tungsten oxide nanoneedles were deposited by AACVD from [$W(OPh)_6$] in a range of organic solvents. We have found that the he morphology of the deposited films depends on the temperature and the solvent used. For enhancing the performance of the sensing layer, we have studied at first, a co-deposition of WO_3 nanoneedles with gold metal nanoparticles, and secondly, we have given an overview about the alignment of nanoneedles by dielectrophoresis, between electrodes as our future work.

1. Introduction

In the last years, a great deal of research has been focused in the development of the sensing layer and the improvement of the sensing properties of nanosensors toward low concentration of different toxics gases.

Sensing layers based on metal oxide thin films have applications in a diverse range of fields including the glazing industry and gas sensing [1]; hence, there is a variety of physical and chemical techniques of deposition of this material including sol–gel, physical vapour deposition (PVD) and Aerosol assisted chemical vapour deposition (AACVD) [1].

In this paper we report the basic principle of AACVD process for the deposition of tungsten oxide nanoneedles using [$W(OPh)_6$] in a range of organic solvents.

Then, we present a co-deposition of tungsten oxide nanoneedles decorated by gold nanoparticles for enhancing the sensitivity and the selectivity of the deposited sensing layer.

Later, we give an overview about our future work, concerning the alignment of nanoneedles between the electrodes with the aim to improve the performance of this kind of sensors.

2. Principe of AACVD

Aerosol assisted chemical vapour deposition (AACVD) is a variant of the CVD process involving the use of liquid–gas aerosols to transport soluble precursors to a heated substrate [1]. The principle of this method is illustrated in figure.1. The precursor is dissolved in a solvent, and then an aerosol is generated ultrasonically. By a carrier gas, the aerosol droplets are transported to the substrate where the surface of reaction is located. The solvent needs to have the right physical and chemical properties for aerosol formation; the precursors do not need to be volatile but just soluble in the solvent. This allows for the use of a wider range of non-volatile precursors, which are not usable in conventional CVD [1-2].

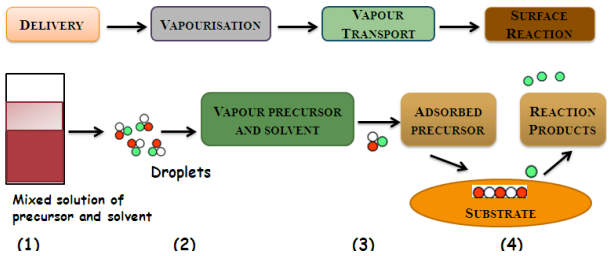

Fig.1.Process of AACVD

3. General synthesis procedure

Tungsten phenoxide[$W(OPh)_6$] (100mg, 6.7 mmol), was dissolved in three types of solvents :20ml of acetone, 20ml of toluene, and a mixture of 10ml acetone and 10ml toluene. Then using a CHICCO ultrasonic humidifier, an aerosol was generated and transported by nitrogen gas onto the heated substrate. The nitrogen gas flow rate of 0.5 l/min^{-1} was constant. The exhaust from the reactor was vented directly into the extraction system of a fume cupboard. The gas flow was continued until all the precursor mix had passed through the reactor, typically 30–50 minutes. The WO_3 nanoneedle was grown in glass substrates at different temperatures between 350C-500C.

4. Results and discussion

By analyzing our samples by scanning electron microscopy SEM (fig.2), we have found that the structure of the deposited films depends on the temperatures and the nature of the solvent used.

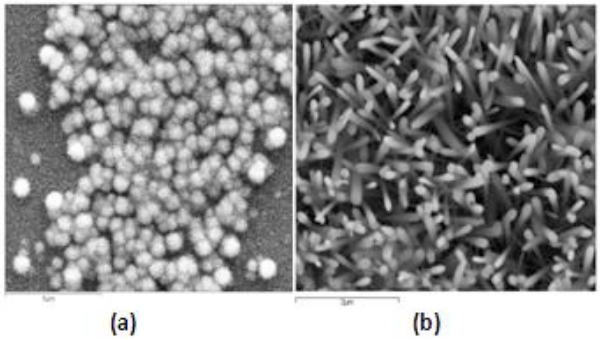

Fig.2. SEM images of WO_3 deposited at: (a) 350C, and (b) 500C using a mixture of acetone and toluene.

At low temperature (fig.2.a), we have agglomeration of WO_3 nanoparticles; however, at higher temperature (fig.2.b), we have WO_3 nanoneedles.
The table below (Tab.1) illustrates the different morphologies observed according to the solvent and the temperature used.

Deposition temperature	WO3 Morphology		
	Acetone	Toluene	Acetone+ Toluene
350	-	-	P
400	P	-	P+N
500	N	N	N

Table.1. Morphology of WO_3 in dependence with temperature and nature of the solvent.

5. Co-deposition of tungsten oxide decorated with gold nanoparticles

For enhancing the performance of the sensing layer, AACVD give us the opportunity to deposit in a single process with a mixture of different precursors, Tungsten oxide nanoneedls decorated by Gold nanoparticles [2].
Figure.3, show the TEM images of particles removed from the substrate by sonication in methanol.

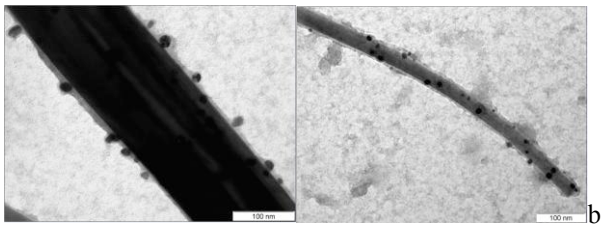

b

Fig.3.TEM images of WO_3 nanoneedls with dispersed gold nanoparticles on the surface

We observe the presence of highly monodisperse gold nanoparticles (approximate diameter 13.10 ± 0.89 nm for a total population) randomly dispersed along the surface of the WO_3 nanoneedles.
By referring to the work that was done in our group [2], sensors based on Au/WO_3 sensing layer, show a high response to low concentration of toxics gases like ethanol, benzene, hydrogen sulfide and others.

6. Dielectrophoresis and alignment of nanoneedles

Deposition of WO_3 nanoneedles on a sensor substrate using AACVD of [$W(OPh)_6$] in the absence of an electric field, produced material with random orientation at the electrode-substrate surface. However, when we applied an electric field across the sensor during deposition, it was observed that extended nanoneedles dominated the morphology. Hence, this phenomena is called Dielectrophoresis (DEP) [3].
By definition, DEP is an electro-kinetic mechanism during which polarizable particles suspended in a fluid medium move under the influence of an electrical field. This electric field is generated by application of an ac voltage between the electrodes and the nature of the electric wave can be sinusoidal, rectangular, etc.
If the suspended particle has a higher polarizability than that of the surrounding fluid medium, then the particles are pushed toward the higher electrical field region. This is called positive dielectrophoresis. However if the suspended particle has a lower polarizability than the surrounding medium, the particle is pushed toward the region of weaker electrical field, and this is called negative dielectrophoresis[3].
The fluid medium can be ethanol, de-ionized water, acetone, etc.
To get a good alignment we should control many other parameters such as gap between electrodes, wave frequency, applied voltage, shapes of electrodes and the nature of the substrate.
Using this method we can ensure good contacts between the electrodes that can enhance the performance of the sensing layer and also it increases the sensitivity and the repeatability of the sensors, towards low concentration of toxics gases.

7. Conclusions

In conclusion, Tungsten oxide nanoneedles have been successfully deposited by AACVD.
We have observed different morphology according to the temperature and the solvent used.
Sensors based on Au/WO_3 nanoneedles have shown a high sensitivity to low concentrations of toxic gases like ethanol, benzene or hydrogen sulfide.
For the alignment of the nanoneedles, we have designed a new reactor allowing us to deposit tungsten oxide in an electric field environment.

References

[1] S. Ashraf et al., "Aerosol assisted chemical vapour deposition of WO_3 thin films from tungsten hexacarbonyl and their gas sensing properties", J. Mat. Chemistry 17, pp. 3708–3713, 2007.
[2] S.Vallejos et al., "Au nanoparticle-functionalised WO_3 nanoneedles and their application in high sensitivity gas sensor devices", Chem. Commun 47, pp. 565–567, 2010.
[3] P.J.Burke, "Nanodielectrophoresis: Electronic Nanotweezers"Encyclopedia of Nanotechnology X, pp. 1-19, 2003.

Film Morphology of the Organic Solar Cells P3HT:PCBM[70]

V.S. Balderrama[a], M. Estrada[b], P. Formentin[a], A. Viterisi[c], J. Ferré-Borrull[a], J. Pallarés[a], E. Palomares[c] and L.F. Marsal[a*]

[a]Departament d'Enginyeria Electrònica, Elèctrica i Automàtica, Universitat Rovira i Virgili, Avda. Països Catalans 26, 43007 Tarragona, Spain

[b]Sección de Electrónica del Estado Sólido, Depto. Ingeniería Eléctrica, CINVESTAV-IPN, Av. IPN No 2508, Apto. Postal 14-740, C.P. 07360, D.F., México

[c]Institute of Chemical Research of Catalonia (ICIQ),. Avda. Països Catalans 16, 43007, Tarragona, Spain

*Corresponding author: L.F. Marsal; email: victorsamuel.balderrama@urv.cat ; phone: (+34) 977 55 96 25.

1. Abstract

In these work, the morphology and performance of Bulk Heterojunction Organic Solar Cells (BHJ-OSC) fabricated with three different ratios of P3HT:PCBM[70] (1:0.84, 1:1 and 1:1.21, wt%) were studied. The films morphology of each OSCs were characterized by atomic force microscopy (AFM). The parameters of the OSC were extracted from current-voltage characteristic (I-V) curve under illuminated conditions.

2. Introduction

At present, the power conversion efficiency in BHJ organic solar cell has been increased up to 8.3% [1]. The development of the film morphology in OSCs is important for obtain a good performance [2]. In the work, the effects of the morphology in devices featuring a ITO/PEDOT:PSS/P3HT:PCBM[70]/Ca/Ag structure were investigated variaying the amount of PCBM[70].

3. Experimental and Results

Blends S1, S2, and S3 were made with 1:0.84, 1:1, and 1:1.2 wt % of P3HT:PCBM[70] respectively and diluted in chlorobenzene:o-dichlorobenzene solution with a ratio of volume (60:40). The blends were then left stirring during 17 h at 50ºC. The films were spin-coated at 45 s at 600 RPM. The thickness of blend layers was of 90 nm. The metal contact used was Ca/Ag and deposited by thermal evaporation and the thickness was of 20 and 200 nm, respectively. We applied an annealing and were done on a hot plate at 135ºC for 20 min under nitrogen atmosphere. The I-V characterization of the devices under light was made at 1sun (100 mW/cm^2) under a N_2 atmosphere at 300 K after fabrication (fig. 1). Table 1 shows the extracted parameters of the devices under light. The layer morphology was characterized using AFM in the tapping mode (fig. 2) and is only shown for the blend film S1. In our experiments, we observed that increasing the PCBM[70] the short circuit current density J_{sc} also increases [3]. The open circuit voltage V_{oc}, remains unchanged for the three types of blend films [4]. Devices fabricated with S1 showed better performance. The appropriate incorporation of PCBM[70] in the blend film consequently assures the formation of ways of percolation [5-6]. The roughness of the S1 blend film was of 0.96 nm.

4. Conclusions

In summary, we have analysed the films morphology change of the OSC of P3HT:PCBM[70] made with 3 different solutions. The proper incorporation of PCBM[70] in the blend is mainly reflected in the parameters of fill factor and short circuit current. Devices fabricated with S1 blend shows the best performance. The morphology of the blend film was showed by AFM.

Acknowledgements

This work was supported by the Spanish Ministry of Science and Innovation (MICINN) under grant number TEC2009-09551, CONSOLIDER HOPE project CSD2007-00007, Catalan authority under project 2009 SGR 549, and the CONACYT 12 7978.

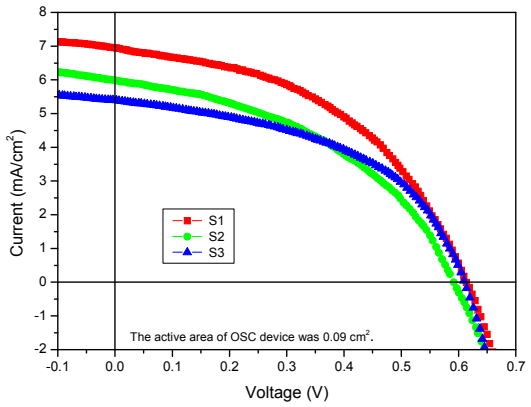

Fig.1. Current – Voltage (I-V) characteristics measured under illumination of the three blends solutions S1, S2 and S3.

No. of Blend under illuminated	wt (%)	Jsc (mA/cm^2)	Voc (V)	FF (%)	η (%)
S1	1:0.84	6.9	0.61	47	2.0
S2	1:1	5.9	0.58	43	1.54
S3	1:1.21	5.3	0.60	48	1.57

Table1. Electrical parameters of all blend films under illumination standard conditions (100 mW/cm^2) 1 sun at 300 K. J_{sc} is the short circuit current density, V_{oc} is the open circuit voltage, FF is the fill factor, and η % is the power conversion efficiency.

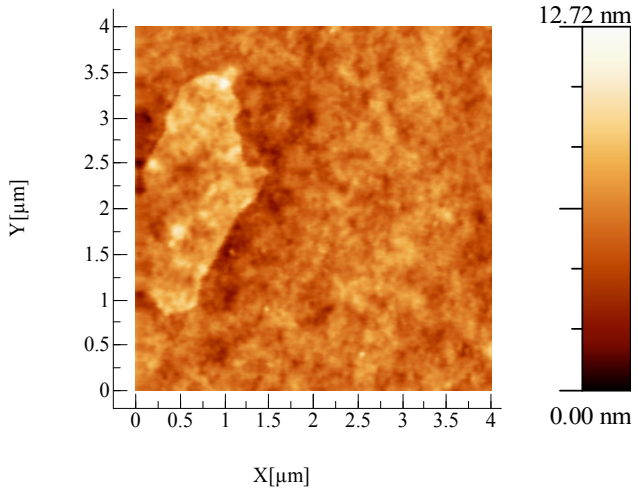

Fig.2. AFM Results for the S1 blend film. Shown is the topography and the value of roughness average was of 0.96 nm.

References

[1] M. Green et al., *Res. Appl. 19*, pp. 84-92, 2011.
[2] Bogyu Lim et al., *J. Mater. Chem. 20*, pp. 10919 - 10923, 2010.
[3] D. Chirvase et al., *Nanotechnology 15*, pp. 1317-1323, 2004.
[4] Tobias Erb et al., *Adv.Funct. Mater,. 15,* pp. 1193 - 1196, 2005.
[5] H. Hoppe et al., *Thin Solid Films 511,* pp. 587-592, 2006.
[6] S.E. Shaheen et al., *Appl. Phys. Letter. 78 ,* pp. 841, 2001.

Study of the correlation between mobility and the density of states in small molecule and polymeric OTFTs

A. Castro-Carranza[1], M. Benwadih[3], R. Gwoziecki[3], Y. Xu[2], M. Estrada[4], A. Cerdeira[4], J. C. Nolasco[1], G. Ghibaudo[2], B. Iñiguez[1] and J. Pallarès[1]

[1] DEEEiA, Universitat Rovira I Virgili; Av. Països Catalans 26, 43007, Tarragona, Spain.
[2] IMEP-LAHC, INP-Grenoble, MINATEC, 3 Parvis Louis Neel, BP 257, 38016 Grenoble, France.
[3] CEA-LITEN, 17 rue des Martyrs, 38052 Grenoble, France.
[4] CINVESTAV-IPN , Av. IPN 2508 Col. Zacatenco 07360, Mexico City.

Abstract

In the present work we analyze the correlation of the field dependent mobility and the distribution of states DOS by means of the electrical characteristics of bottom contact OTFTs with three different active layers: two with small molecule materials, i.e. the P-type 6,13-bis(triisopropylsilylethinyl)Pentacene (***tips-Pentacene***) and the N-type N,N-dialkylsubstituted - (1,7 & 1,6) – dicyanoperylene - 3,4 : 9,10 - bis(dicarbiximide) derivative (***Polyera Activink^{TM} N1400***); and one polymer, i.e. and the P-Type Poly(Triarylamine) (***PTAA***).

1. Introduction

Due to the potential applications Organic Thin Film Transistors (OTFTs) have revealed up to now, new materials, from small molecule to polymers, have been synthesized in order to improve the performance of these devices. It is known that solution processed semiconductors have defect states intrinsically due to the amorphous nature, as well as intrinsic impurities in the layers. Also small molecule organic materials are affected by defect states; however the nature of such defects is not trivial. In general these states are localized between the HOMO and LUMO levels of the organic materials and they affect the conduction mechanisms through trapping and detrapping of charge which affect the transistor mobility.

In this study we analyze the effect of shallow traps on the mobility of bottom contact OTFTs with three different active layers as previously mentioned: two with small molecule materials, the P-Type *tips-Pentacene* and the N-type *Polyera Activink N1400*; and one P-Type polymer i.e. *PTAA*. The chemical structures of these materials are shown in Fig.1.

2. Characterization and Modeling

The OTFTs under study with dimensions T1 (L= 50 µm, W= 200 µm) and T2 (L= 20 µm, W= 500 µm) were fabricated in CEA-LITEN with an already reported technological process [1, 2]. The schematic structure is shown in Fig. 1.

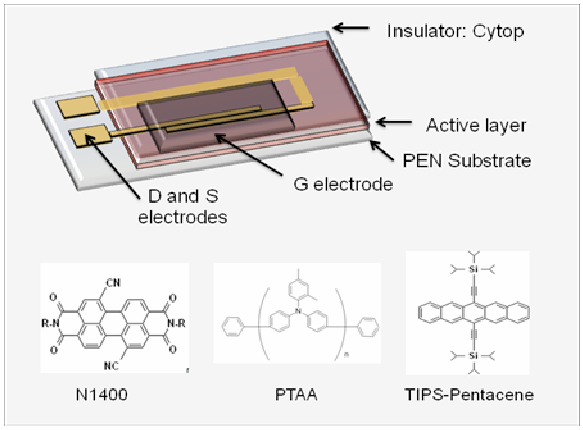

Fig.1. Schematic design of the fabricated staggered bottom contact OTFTs and chemical structures of the three applied semiconductors in the active layer.

All devices showed ohmic contact checked by the slope of the lin-lin representation of their output characteristics respectively

For extracting the DOS and mobility parameters from the electrical characteristics of the devices, the Unified

Model and Extraction Method ***UMEM*** [3] was applied.
UMEM allows the easy calculation of the characteristic temperature T_0 and the density of localized states, considering an exponential distribution of traps and a concentration of localized charge much greater than free one in all operation regimes.
In this method, the considered field effect mobility is represented with the power law [4]:

$$\mu_{FET} = \frac{\mu_0}{Vaa^{\gamma}}\left(V_{GS} - V_{FB}\right)^{1+\gamma} \qquad (1)$$

where V_{GS} is the gate-to-source voltage, V_{FB} the flat band voltage and $\frac{\mu_0}{Vaa^{\gamma}}$ represents the mobility at (V_{GS} - V_{FB})=1 V.

γ depends on the characteristic temperature T_0 , associated with the disorder within the material.

Fig. 2 shows the experimental and modeled output characteristics of four studied OTFTs with different already mentioned semiconductors. A good fitting was obtained for two $|V_{GS}|$ values.

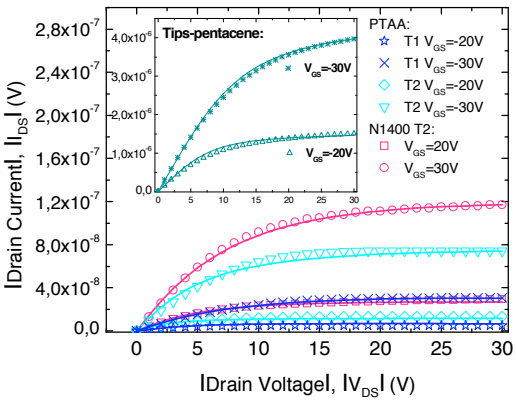

Fig.2. Experimental (symbols) and modeled (straight lines) output characteristics at $|V_{GS}|$=20 V and 30 V.

The mobility for the three materials is obtained as well, as shown in Fig.3

3. DOS

After extracting parameters, plots of the field dependent mobility (2) and the distribution of states DOS (3) can be obtained.
The concentration of localized states gd_0 is also extracted using the device geometry, temperature, and gate voltage overdrive dependent mobility expression obtained in [3] for the I_{DS} model. Together, T_0 and gd_0 determine the exponential function of the distribution of localized states DOS given by (2), Fig 4.

$$g_d(E) = g_{d0}\exp\left(-\frac{E}{E_0}\right) \qquad (2)$$

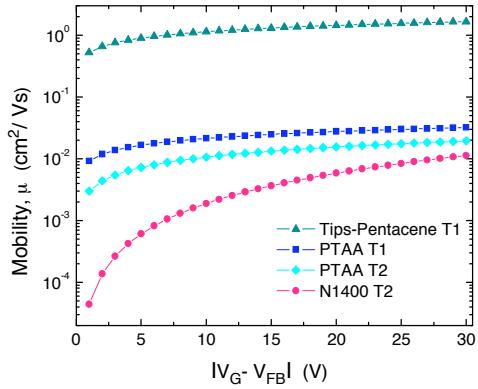

Fig. 3. $|V_{GT}|$ dependent mobility of the analyzed organic semiconductors.

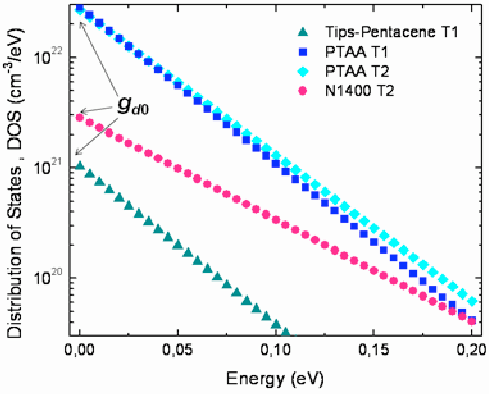

4. Conclusions

We found some relations between the DOS parameters and mobility, specifically that the dependence of mobility on voltage is related to the characteristic energy of the material and that magnitude of mobility depends mainly on gd0.
Although the mobility of TIPS-Pentacene is higher than PTAA, the dependence on V_{GS} for both kinds of transistors is similar. It was attributed to their similar E_0 ≈ 0.03 eV.
The lower mobility in PTAA is related to g_{d0} which is higher than the TIPS-Pentacene one, as shown in Fig. 5.
There is a higher dependence of mobility on V_{GS} for the Polyera Activink N1400 transistors. At higher V_{GS} such mobility enhances around three orders of magnitude. This is attributed to its E_0 ≈ 0.05 eV.

References

[1] D. Boudinet et al. Organic Electronics, 11, 227-237 (2010).
[2] J.M. Verilhac et al. Organic Electronics, 11, 456-462 (2010).
[3] M. Estrada et al., Solid State Electron, 52, 787-792 (2008).
[4] Fjeldly TA, et. al., Wiley Interscience, New York, 1998

Compact Models of the Gate Leakage Current for the Selection of High-*k* Gate Dielectrics

G. Darbandy[1], F. Lime[1], A. Cerdeira[2], M. Estrada[2], S. I. Garduño[2] and B. Iñiguez[1]

[1] Departament d'Enginyeria Electrònica, Elèctrica i Automàtica, Universitat Rovira i Virgili, Spain.
[2] Sección de Electrónica del Estado Sólido, Depto. Ingeniería Eléctrica, CINVESTAV-IPN, México D.F.

1. Abstract

Analytical models of the direct tunneling gate leakage current based on a proper description of the WKB tunneling probability and validated by TCAD simulation, were presented to determine the most promising dielectric materials for fully depleted UTB SOI MOSFETs with Equivalent Oxide Thickness (EOT) values and maximum values of gate leakage current according to the requirements of latest ITRS roadmap for two technological nodes.

2. Introduction

One of the key elements that allowed the successful scaling down of silicon based MOSFETs is the suitability of high *k* materials as a gate oxide dielectric. In fact the gate leakage tunneling current can be suppressed by using suitable high *k* dielectric materials [1, 2]. In our previous works we have studied the suitability of high *k* materials in Double-Gate SOI MOSFETs structure for the 22 nm node requirements assuming an ideal interface without any interfacial layer [3] and SiO_2 as an interfacial layer [4].
In this work, we have developed analytical models for the direct tunneling gate leakage current [5] through gate stacks based on a proper description of the WKB tunneling probability adapted to UTB SOI MOSFETs structure and we incorporate it to our new compact model for the potential and drain current of a UTB SOI MOSFET [6].

3. Simple analytical model with and without interfacial layer

A simple analytical model that includes some approximations for the direct tunneling leakage flowing between gate and channel as the main gate leakage component [5], using our new compact model of a UTB SOI MOSFET, was developed for the required conditions according to the requirements of ITRS (ITRS 2009) for the next generations of UTB SOI MOSFETs. The effects of the EOT, gate leakage current, electron effective mass in the high *k* dielectric materials (m^*), dielectric constant *k* value, barrier height and SiO_2 thickness as an interfacial layer were studied using the considered developed gate leakage tunneling current expressions.

4. Improved analytical model with and without interfacial layer

An improved analytical model can be obtained from the simple model by adding a correction function in order to take into account some effects that were not properly included in the simple model and lead to inaccuracies [7]. The direct tunneling gate leakage current as a function of gate voltage at $V_d = 0$ obtained by calculation of our model and TCAD numerical simulations is shown in Fig.1. There is a good agreement between model and simulation results.

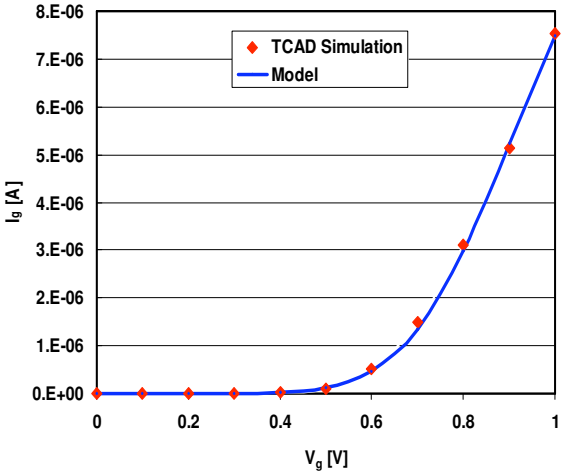

Fig.1: Analytical model calculation and TCAD simulation for the gate leakage tunneling current for UTB SOI MOSFET.

5. Results and discussion

We studied suitable high *k* materials by plotting band offset versus dielectric constant using the models for the considered conditions. Fig. 2 and Fig.3 show the most promising dielectric candidates for the given parameters (mentioned in the captions) and latest ITRS requirements for two next generations of UTB SOI

MOSFETs in the case of one layer and two layer gate insulators. Fig.3 shows that the most suitable dielectric candidates are such as HfO_2, ZrO_2 and La_2O_3 for the 14nm and 15nm nodes in the case of two layers insulators. The alternative dielectrics should satisfy the mentioned requirements.

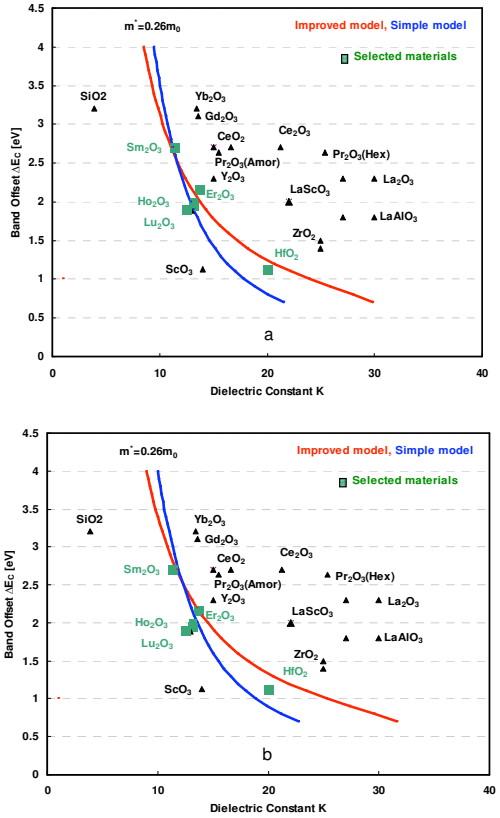

Fig.2: Band offset as a function of k-value, for (a) 15nm node: EOT=0.85nm and J= 0.21 [A/cm^2] and (b) 14nm node: EOT=0.8nm and J= 0.23 [A/cm^2] according to ITRS at V_g = 1 V, $m^*=0.26m_0$ and V_d = 0 without interfacial layer.

6. Conclusion

Analytical models of the gate tunneling leakage were developed to determine the most promising high *k* candidates for the UTB SOI MOSFETs structure for the requirements of low standby power applications according to the latest ITRS roadmap. Various issues/factors that need to be considered while replacing gate oxide materials have been studied to meet the requirements. Finding suitable materials depends on the technology node requirements and especially EOT, the electron effective mass and interfacial layer thickness, which can change the choice of the right dielectric candidate. HfO_2 and Lu_2O_3 are the most promising materials for the 14nm and 15nm nodes requirements assuming ideal case without interfacial layer.

Acknowledgements

This work was supported by Ministerio de Ciencia e Innovación under project TEC2008-06758-C02-02, by the European Commission under Contract No. 216171 "NANOSIL", and FP7-PEOPLE-2007-3-1-IAPP No. 218255 "Compact Modelling Network (COMON)" and No. 216373 "EUROSOI", by the ICREA Academia Award and by the PGIR Grant from URV.

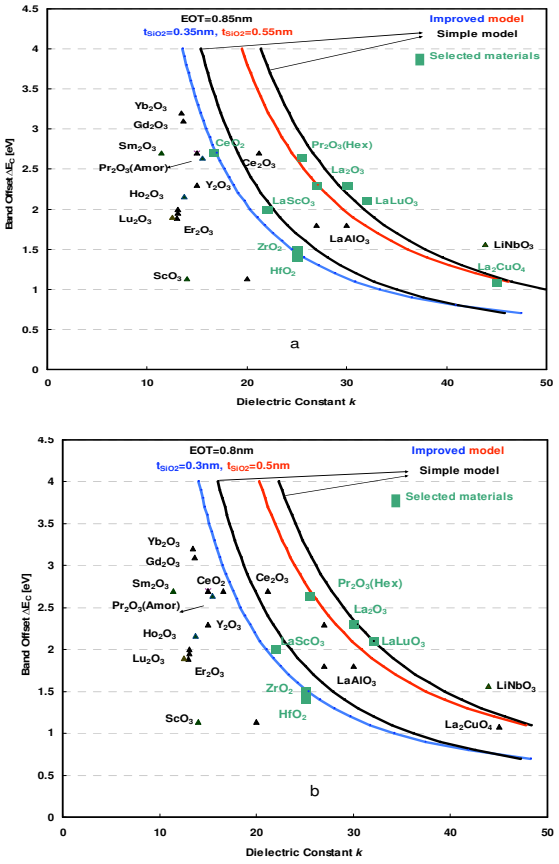

Fig.3: Band offset as a function of k-value for (a) 15nm node: EOT=0.85nm and J= 0.21 [A/cm^2] and (b) 14nm node: EOT=0.8nm and J= 0.23 [A/cm^2] according to ITRS at V_g = 1 V, $m_{sio2}=0.50m_0$, $m^*=0.26m_0$ and V_d = 0 with SiO_2 as an interfacial layer.

References

[1] M. Depas et al, *Solid-State Electron.* **38** (1995) 1465

[2] M. H. Chowdhury et al, *IJETSE*, Vol **2**, July 2010

[3] G. Darbandy et al, *Solid-State Electronics,* **54** (2010), pp. 1083-1087

[4] G. Darbandy et al, *Semicond. Sci. Techno.* **25** (2010)

[5] T. Kauerauf et al, *Solid State Electron* 2005; **49** (5): 695–701.

[6] F. Lime et al, *Solid-State Electronics* 57 (2011) 61–66

[7] W-C. Lee et al, *IEEE Trans Electron Dev* 2001; **48** (7):1366-1373.

FDTD Evaluation of Light Propagation Properties in Two-dimensional Nanostructured Organic Solar Cells

Pedro Granero, Josep Ferré-Borrull, Josep Pallarès and Lluís F. Marsal *

Nano-electronic and Photonic Systems - NePhoS, Universitat Rovira i Virgili,
Avda. Països Catalans 26, 43007 Tarragona, Spain.
* Voice: +34977559625, Fax: +34977559605, E-mail address: lluis.marsal@urv.cat

Abstract

Nanostructured organic solar cells (OSC) join the advantages of bilayer devices and bulk heterojunction cells. They provide a high interface area between the active materials and direct paths for carriers' collection. However, this architecture can also be advantageous in terms of light absorption. By means of FDTD simulations, we investigate light propagation, absorption and reflection in nanostructured OSC.

1. Introduction

Nowadays organic solar cells (OSC) are less profitable than traditional polluting energy sources. One of the main problems is the short exciton diffusion length that organic materials have. This causes that only those excitons generated close to a Donor-Acceptor interface can dissociate and contribute to photocurrent.

A solution to this is the ordered bulk heterojunction (BHJ) or nanostructured cell, which joins the advantages of bilayer OSC together with the BHJ cell ones [1]. So we have a device that offers spatially uninterrupted pathways to electrodes (bilayer cells) and suitable distances for short exciton diffusion lengths (BHJ cells). However, these improvements in the electrical behavior may not be the only benefit that this kind of cells can offer.

The fact that the structuring has subwavelength dimensions suggests that there can be an increase in light absorption due to light trapping within the device. Several studies demonstrate this fact by using surface plasmons in dielectric-metal unions [2] or hybrid cells [3]. However, this phenomenon seems to not have been exhaustively studied in OSC.

In this communication we are going to simulate nanostructured cells and to evaluate changes in absorption as a function of the geometrical parameters.

2. The Computational Domain

Our simulations are based in Meep, which is a free finite-difference time-domain (FDTD) simulation software [4]. The used 2D-computational domain is shown in Figure 1. The OSC that we want to study is placed on the right of the computational domain and consists in a 4 μm-width and 40 nm-thick cell. Variations in material composition are in the x- and y-directions, while the cell in infinite in the z- direction. The device is composed of 3 layers. The outmost layers are 10 nm width and homogeneous, being the one of the left of poly(3-hexylthiophene) (P3HT) and the one of the right of 1-(3-methoxycarbonyl)-propyl-1-phenyl-(6,6)C_{61} (PCBM). The inner layer represents the nanostructuring and consists of a periodic succession of P3HT and PCBM blocks with thickness 20 nm and height a, as indicated in Fig. 1. A source emitting a plane wave with a Gaussian spectrum centered at 500 nm is placed at the left of the computational domain. In order to evaluate the amount of light reflected, transmitted and absorbed by the cell, the average electromagnetic flux through two lines placed in front and after the cell (indicated as Detec. 1 and Detec. 2 in Fig. 1) is registered. The reflectance, absorption and transmittance are obtained by comparison with the fluxes registered in the absence of the cell. The results are then compared with those of an equivalent planar bilayer cell. We also are going to use another reference cell where the nanostructured layer is replaced with an effective medium which combines the optical properties of P3HT and PCBM.

3. Results and Discussion

The reflectance of the nanostructured OSC as a function of the parameter a is shown in Fig. 2. The reflectance values of the reference planar bilayer and the effective-medium cells are indicated by the long-dashed and by the short-dashed lines respectively. As it can be seen, nanostructuring reduces the reflection in all cases. The maximum reduction reaches an 8.61% if compared with the planar reference cell. This result is achieved when a is 40 nm. However, Fig. 2 also shows that the reflection is almost not dependent on a in all the studied range of values. Moreover, we also can see that all reflectance values are similar to the effective-medium cell one. These facts suggest that, from the point of view of

reflectance, nanostructuring has a behavior that remains close to that one of an effective medium.

Fig. 3 shows light absorption as a function of *a*. Unlike reflectance, now the dependence with *a* is greater: the difference between the highest and the lowest value of absorbance is now of 6.68%. It can also be seen that absorbance decreases with increasing *a*, becoming lower than for the planar cell for *a* greater than 40 nm. Consequently, not all geometries improve the behavior of the cell. In this simulation, the better value of light absorption, corresponding to an increase of 5.42% with respect to the planar cell, is achieved for $a = 5$ nm.

Despite this worsening in absorbance at big values of *a*, it should be kept in mind that it only represents a decrease of a 1.62% (worse value) if compared with the planar bilayer cell. Moreover, as it can be deduced from Fig. 3, the decrease rate is smaller as *a* becomes greater. These facts suggest that for bigger nanostructure periods light absorption remains the same as for the reference planar bilayer cell.

4. Conclusions

In this work we have investigated light propagation in nanostructured organic solar cells by means of FDTD simulations. Our results have shown that nanostructuring can reduce reflection significantly. However, this reduction is quite independent of the nanostructuring features. This indicates that the nanostructured layer acts as an effective medium for the reflected light. Regarding to light absorption, we have found that the dependence of the absorbance with *a* is much bigger than the dependence of the reflectance was. For small values of *a*, nanostructuring increases absorption but for big values it decreases it until the absorption improvement is cancelled (if compared with a reference planar bilayer cell). So, we have shown that nanostructuring can improve light absorption.

ACKNOWLEDGMENT

This work was supported by the Spanish Ministry of Science and Innovation (MICINN) under grant number TEC2009-09551, CONSOLIDER HOPE project CSD2007-00007, AECID project A/024560/09, and by the Catalan Authority under project 2009SGR549.

References

[1] H. Hoppe, and N. S. Sariciftci, "Organic Solar Cells: An Overview", *J. Mater. Res.*, vol. 19, issue 7, pp. 1924-1945, Jul. 2004.

[2] H. A. Atwater, and A. Polman, "Plasmonics for Improved Photovoltaic Devices", *Nature Materials*, vol. 9, issue 3, pp. 205-213, Mar. 2010.

[3] J. R. Tumbleston, D. H. Ko, E. T. Samulski, and R. Lopez, "Absorption and Quasiguided Mode Analysis of Organic Solar Cells with Photonic Crystal Photoactive Layers", *Optics Express*, vol. 17, issue 9, pp. 7670-7681, Apr. 2009.

[4] S. G. Johnson, J. D. Joannopoulos, and M. Soljačić, "Nanostructures and Computation Wiki," Massachusetts Institute of Technology. Available: http://ab-initio.mit.edu/wiki/index.php/Main_Page.

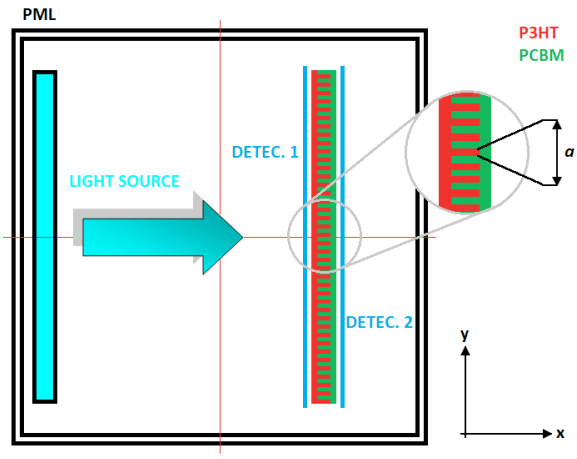

Fig.1. Scheme of the used computational domain displaying the light source, the cell and the detectors. It also shows the perfectly matched layer (PML) that avoids interferences from domain boundaries.

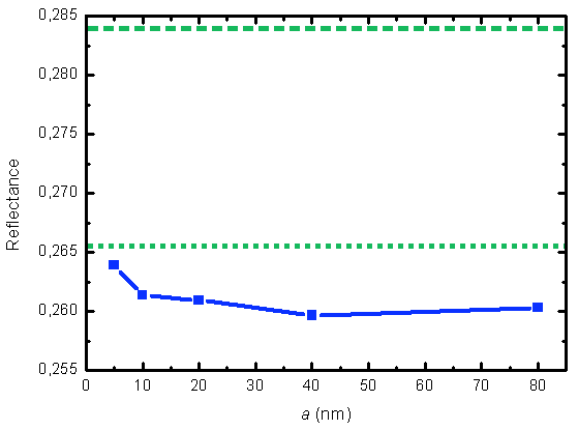

Fig.2. Reflectance values of the simulated devices as a function of *a*. The long-dashed line and the short-dashed line correspond to the planar bilayer cell and to the effective-medium cell respectively.

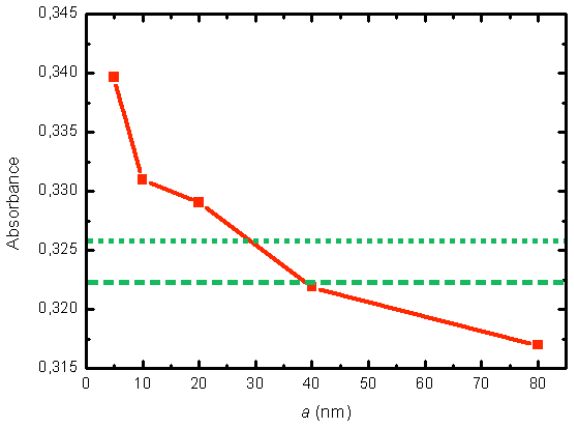

Fig.3. Absorbance values of the simulated devices as a function of *a*. The long-dashed line and the short-dashed line correspond to the planar bilayer cell and to the effective-medium cell respectively.

2D Analytical Modeling of the Potential in Doped DG-MOSFETs including Inversion Charge

Thomas Holtij[1,2,✠], Mike Schwarz[1,2], Alexander Kloes[1] and Benjamín Iñíguez[2]

[1]Technische Hochschule Mittelhessen, Giessen, Germany
[2]Universitat Rovira i Virgili, Tarragona, Spain
✠thomas.holtij@ei.th-mittelhessen.de

***Abstract*— In this paper, we present a physics-based analytical model for the calculation of the electrostatic potential within doped short-channel DG-MOSFETs including inversion charge. To calculate the potential, we make use of the Schwarz-Christoffel transformation. A comparison with our calculations has been done versus TCAD Sentaurus.**

***Index Terms*— Analytical modeling, conformal mapping, DG-MOSFET, potential solution, inversion charge, doping**

I. Introduction

Ultrathin-film body DG-MOSFETs are considered to be very attractive options to improve the performance of CMOS devices. They provide a very good electrostatic behavior to overcome the short-channel effects (SCEs) encountered by downscaling the devices into the sub $32nm$ region, as for example the threshold voltage roll-off, the subthreshold slope degradation and the drain-induced barrier lowering (DIBL). Due to the SCEs the off-state leakage current increases. In DG-MOSFETs, the control of the channel is stronger than in bulk MOSFETs. Thus, the SCEs are reduced [1].

Up to now, most of the presented compact models do only consider undoped long-channel devices. However, due to technological constraints in real devices, one always faces the problem of having dopants inside the channel which influence its electrostatic behavior. Dopants can cause a threshold voltage shift, make the subthreshold slope worse and reduce the carrier mobility [2]. Hence, there is an urgent need for compact models which are able to predict the electrostatic behavior of such, especially short-channel, devices.

In this paper, we focus on the DG-MOSFET because it is a leading candidate to replace the conventional bulk MOSFET. In order to calculate the potential, we present a first two-dimensional approach from which an analytical model has been derived by using the Schwarz-Christoffel transformation [3]. In this work we assume an enhancement n-type DG-MOSFET and focus on a bias of V_{ds}=0V.

II. Calculation of the Potential

Inside the channel region the Poisson equation reads as

$$\Delta\phi(x,y) = -\frac{\rho}{\epsilon} = -\frac{qN_B}{\epsilon_{Si}} - \frac{q_{inv}}{\epsilon_{Si}}, \tag{1}$$

whereby q is the elementary charge, N_B the doping concentration, q_{inv} the mobile charge density and ϵ_{Si} the permittivity of silicon. Now, in order to calculate the potential, the solution of Poisson's equation is decomposed into a one-dimensional particular solution $\phi_p(y)$, and a two-dimensional part $\varphi(x,y)$ which represents the 2D solution of the homogeneous Laplacian differential equation.

$$\Delta\phi(x,y) = \Delta\varphi(x,y) + \Delta\phi_p(y) \tag{2}$$

with

$$\Delta\varphi(x,y) = 0 \quad \text{and} \quad \Delta\phi_p(y) = -\frac{qN_B}{\epsilon_{Si}} - \frac{q_{inv}}{\epsilon_{Si}}. \tag{3}$$

This decomposition allows us to apply the conformal mapping technique to the Laplacian part only, which is more easy to solve compared to Poisson's equation due to the absence of the space charge ρ. Using this approach, ρ has to be constant along the x-direction [4]. Figure 1 illustrates the used DG-MOSFET structure. For the calculations the source/drain

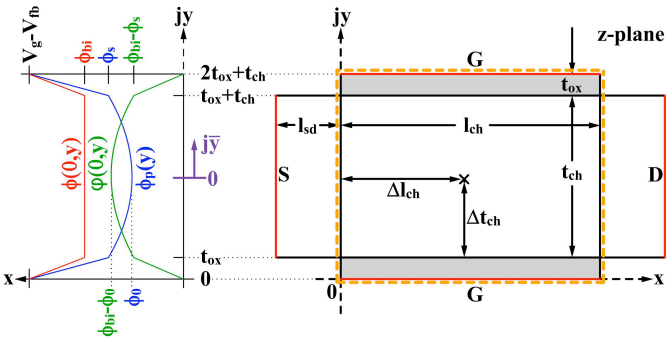

Figure 1. Ideal structure of a DG-MOSFET in complex plane z, wherein Poisson's equation is solved. The corresponding potentials of the decomposed equation (2) at the position (x=0,y) are depicted besides.

areas are cut out. To further ease the problem, the structure is cut into 2 two corner problems to keep the mathematics simple (Fig. 2) [5]. To avoid a discontinuity of the electric field at the Si-SiO2 interface, an equivalent oxide thickness $\tilde{t}_{ox}$=$\epsilon_{Si}t_{ox}/\epsilon_{ox}$ is introduced.

Afterwards, the Schwarz-Christoffel transformation is applied to map the inside of the polygon from Fig. 2 (complex z-plane) to the upper half of the complex w-plane wherein all boundaries are located on the real axis. Now, the potential can be solved more easily. In the upper half of the complex w-plane a potential solution with an infinitesimal gap at position $\overline{u}$ for two electrodes along the real axis is applied [3], which is stepwise superposed to obtain the boundary conditions given in Fig. 2 [5].

$$P = \Phi + j\Xi = d\varphi + j\frac{d\varphi}{\pi}\ln(w-\overline{u}) \tag{4}$$

The boundary condition within the oxide is linearly approximated [5]. The surface potential ϕ_s and the potential in the

middle of the channel ϕ_0 can be derived from solving 1D Poisson's equation in an long-channel device.

$$\phi_s = V_g - V_{fb} - V_{ox} \tag{5}$$

with

$$V_{ox} = \frac{qN_B t_{ch}}{2}\frac{t_{ox}}{e_{ox}} + \frac{Q_{inv}t_{ox}}{\epsilon_{ox}}, \tag{6}$$

where Q_{inv} is the inversion charge in the channel per unit area. If we further assume this mobile charge to be concentrated in a charge sheet at the silicon surface and V_{ds}=0V, we can approximate the particular solution within the channel by taking into account only the charge of dopants. Then the potential ϕ_0 in the middle of the channel is calculated from the one-dimensional particular solution:

$$\phi_p\left(y = tch/2 + \tilde{t}_{ox}\right) = \frac{qN_B}{2\epsilon_{Si}} \cdot \overline{y}^2 + \phi_0\Big|_{\overline{y}=\frac{t_{ch}}{2}} = \phi_s \tag{7}$$

and consequently

$$\phi_0 = V_g - V_{fb} - V_{ox} - \frac{qN_B t_{ch}^2}{8\epsilon_{Si}}. \tag{8}$$

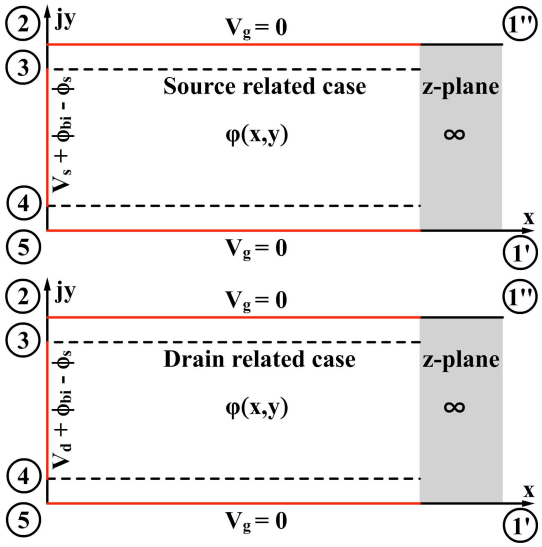

Figure 2. Channel region from Fig 1. The source and drain related cases with its associated boundary conditions are shown in z-plane. The most important points for the conformal mapping are marked.

The inversion charge Q_{inv} is modeled by an expression obtained in [6], which is originally only valid for undoped devices. However, if in strong inversion Q_{inv} gets higher than the channel charge by dopants it is reasonable to apply this equation also for doped devices. The following plots show that when the device operates in strong inversion mode, the potential gets saturated as it should be.

When all calculations have been done, the solution from the source and drain related case are superposed. Finally, the particular solution is added to the two-dimensional Laplacian solution to get the final result.

III. Results

So far, our model is compared versus numerical results from TCAD for a 22nm device having a doping concentration N_A=1e18cm^{-3} and V_{ds}=0V. The model is in good agreement with TCAD except in accumulation and strong inversion region (Fig. 3). Until now, mobile charge in accumulation has not been considered in the model. When the device gets into strong inversion, the accuracy close to the source/drain ends of the channel is less because the same inversion charge density along the whole channel has been used to define the 1D particular solution. (Fig.4). Nevertheless, the model gives reasonable results for the height of the potential barrier from subthreshold to above threshold operation.

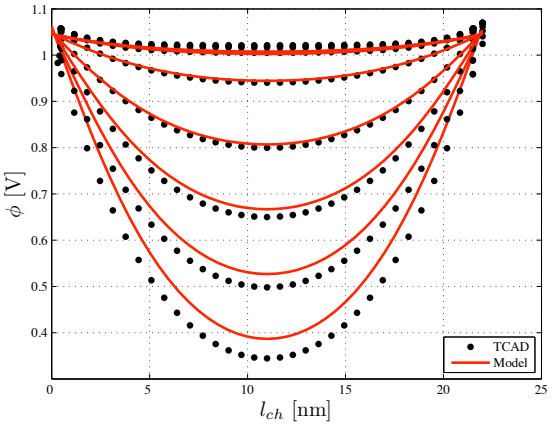

Figure 3. Potential for a slice along the x-axis in the middle of the channel. Parameters: N_A=1e18cm^{-3}, V_{gs}=-0.4V to 1.2V, stepping 0.2V, V_{ds}=0V, l_{ch}=22nm, l_{sd}=10nm, t_{ch}=10nm, t_{ox}=2nm.

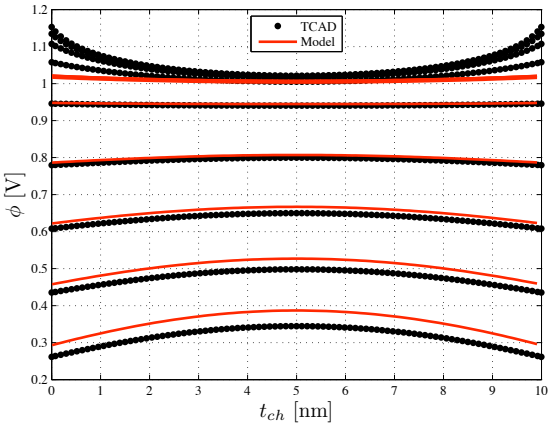

Figure 4. Potential for a slice along the y-axis in the middle of the channel. Parameters: refer to Fig 3.

IV. Acknowledgement

This project was supported by the German Federal Ministry of Education and Research under contract No. 1779X09, by the German Research Foundation (DFG) under Grant KL 1042/3-1, and by the European Commission under FP7 Projects ICT-216171 ("NANOSIL") and IAPP-218255 ("COMON"), by the Spanish Ministerio de Ciencia y Tecnología under Projects TEC2008-06758-C02-02/TEC, by the PGIR/15 Grant from URV and also by the ICREA Academia Prize.

References

[1] B. Iniguez, T. A. Fjeldly, A. Lazaro, F. Danneville, and M. J. Deen, "Compact-Modeling Solutions For Nanoscale Double-Gate and Gate-All-Around MOSFETs," vol. 53, no. 9, pp. 2128–2142, 2006.

[2] H. Lu, W.-Y. Lu, and Y. Taur, "Effect of body doping on double-gate MOSFET characteristics," *SEMICONDUCTOR SCIENCE AND TECHNOLOGY*, vol. 23, 2007.

[3] Weber, *Electromagnetic Fields*. Wiley, 3 ed., 1950.

[4] A. Klös and A. Kostka, "A new analytical method of solving 2D Poisson's equation in MOS devices applied to threshold voltage and subthreshold modeling," *Solid-State Electronics*, vol. 39, no. 12, pp. 1761 – 1775, 1996.

[5] M. Schwarz, M. Weidemann, A. Kloes, and B. Iñíguez, "2D analytical calculation of the electrostatic potential in lightly doped Schottky barrier Double-Gate MOSFET," in *Solid State Electron*, 2010.

[6] B. Iniguez, D. Jimenez, J. Roig, H. A. Hamid, L. F. Marsal, and J. Pallares, "Explicit continuous model for long-channel undoped surrounding gate MOSFETs," vol. 52, no. 8, pp. 1868–1873, 2005.

A high area planar microhotplate pre-concentrator and its application to VOCs monitoring

H. Lahlou[1], X. Vilanova[1], E. Llobet[1], V. Fierro[2], A. Celzard[2], I. Gràcia[3], C. Cané[3], X. Correig[1]

[1] *Departament d'Enginyeria Electronica, Electrica i Automatica, Universitat Rovira i Virgili, Avinguda Països Catalans 26, 43007 Tarragona, Spain*

[2] *Institut Jean Lamour - UMR CNRS 7198, CNRS - Nancy-Université - UPV-Metz, Département Chimie et Physique des Solides et des Surfaces. ENSTIB, 27 rue Philippe Séguin, BP 1041, 88051 Épinal cedex 9, France*

[3] *Gas Sensors Group, National Centre of Microelectronics, CNM CSIC, Campus UAB, 08193 Bellaterra, Spain*

Abstract

A high area microhotplate-based pre-concentrator designed for volatile organic compounds (VOCs) pre-concentration was built and characterized. The performance of the device was validated for the pre-concentration of VOCs, and preliminary results with benzene are presented. This device provides a narrow desorption pulse with an excellent adsorption capacity towards benzene, among the best reported in the literature. Thanks to the low sensitivity of the selected activated carbon to moisture adsorption, the preconcentrator response towards benzene was not affected by humidity. These results make this microconcentrator a promising injection unit for applications with microchromatographic detection systems for a sensitive and selective analysis of benzene in air quality monitoring applications.

1. Introduction

Benzene is one of the most studied volatile organic compounds in the literature due to its carcinogenic effects at very low concentrations [1]. Occupational exposure to this vapour is likely to occur in air from petrochemical manufactures or stations, from automobile exhaust, etc.

One way to enhance the sensitivity of current detection devices towards this compound is to provide some kind of pre-concentration. The main microfabricated structures reported so far include planar hotplates and three-dimensional structures [2]. The three dimensional offers high preconcentration capability due to the high amount of absorbing material which can be hosted by the structure. By exchange, the planar structure is a more simpler fabrication option with limited concentration factors, with low power consumption and better thermal insulation of the structure.

For the special case of benzene, only one work was reported on its pre-concentration with a planar configuration in 1999 [3]. In this case, a concentration factor up to 100 was achieved with a power consumption of 105 mW.

The preconcentration capacity of the planar structure is expected to be further enhanced by choosing an adsorbent having a high adsorption capacity, such as activated carbon.

2. Experimental

2.1. Device fabrication

The microfabricated device is based on a planar membrane of total area 2 mm × 4.5 mm, shown in Fig. 1. This membrane consists of a 1.2 µm thick SiO_2/Si_3N_4 dielectric layer, which was backside anisotropically etched in a 300 µm silicon substrate. A 5 µm thick highly doped silicon plug diffuser is kept under the membrane to further improve temperature homogenization in the heater area. A 0.25 µm thick platinum heater layer was deposited by sputtering over an area of 1.5 mm × 4 mm. It consists of three spiral-shaped heaters which were defined by lift off. A layer of titanium was deposited prior to platinum in order to promote the heater adhesion to the substrate. [4].

The design of the heater was already optimized to have a homogeneous distribution of temperature in the heater active layer with good electro-thermal features, allowing low power consumption (1.02 mW/ ºC) [4].

Activated carbon was selected as adsorbing layer after some previous works which demonstrated its high adsorption capacity towards benzene [5-6]. The preparation and the main characteristics of this material were described elsewhere [5]. The adsorbing layer was drop-coated over the membrane by mixing the activated carbon powder with glycerol with a ratio of 0.5 mg per µL. After the thermal treatment, the total amount of

* Corresponding author
Postal address : Avda Països Catalans, 26
Tel: + 34977256572 ; Fax: + 34977559605
E-mail: houda.lahlou@urv.cat

adsorbent deposited was estimated at 0.25 mg.
The microhotplate preconcentrator was placed in an experimental characterization system based on mass spectrometry described elsewhere [5]. And the concentration factor of the device towards benzene was determined using the procedure described in [5].
Due to its structure similarity with benzene, toluene is likely to interfere with benzene in ambient air. So, it is importance to study the effect of interference between both compounds in the preconcentrator. In order to check this effect, the adsorption capacity of benzene analyzed alone was compared with the case when benzene was mixed with 150 ppb of toluene.
The effect of humidity on the preconcentrator response towards benzene is also important as in real application, the humidty rate in air can vary and cause the breakthrough of the adsorbent. For these analysis, the mass spectrometer was replaced by a commercial Taguchi gas sensor TGS-822 from Figaro. To evaluate the effect of moisture on the preconcentrator response to benzene, the sensor response to 500 ppb of benzene with and without concentrator was studied at different relative humidity (RH): 10, 50 and 75 % RH. The sensor response without the preconcentrator was calculated as the difference between the steady state resistance reached by the sensor while the analyte was flowing to the concentrator/sensor system in the adsorption stage and the baseline resistance. On the other hand, the response to the desorbed analyte was calculated as the difference between resistance at the maximum of desorption peak and baseline resistance.

3. Results and discussion

3.1 Study of the microconcentrator performances towards benzene and toluene

The desorption of benzene from the preconcentrator is completed in less than 3 min, with width at half maximum of about 10 sec, which is a quite narrow injection pulse for gas detection applications.
Figure 1 shows the study of the adsorption capacity of benzene at different initial concentrations in the presence of toluene at equal proportion and at a fixed concentration of 150 ppb of toluene. It can be clearly seen that the adsorption capacity of benzene decreased in the presence of toluene. However, this decrease is negligible for concentrations lower than 300 ppb. Then, the adsorption interference effect between benzene and toluene is expected to be negligible in real conditions.
Figure 2 shows the plot of the sensor resistance in the presence of 500 ppb of benzene, with and without the preconcentator, versus relative humidity. Moisture seems to have no effect on the behaviour of the concentrator towards benzene, since the drop in the sensor response caused by the presence of humidity is the same with and without the preconcentrator. This is an excellent result which confirms the validity of the concentrator based on activated carbon to be operated in ambient air independently from the presence of humidity. This result is explained by the experimental conditions and the extremely low amount of oxygenated surface groups of the selected activated carbons.

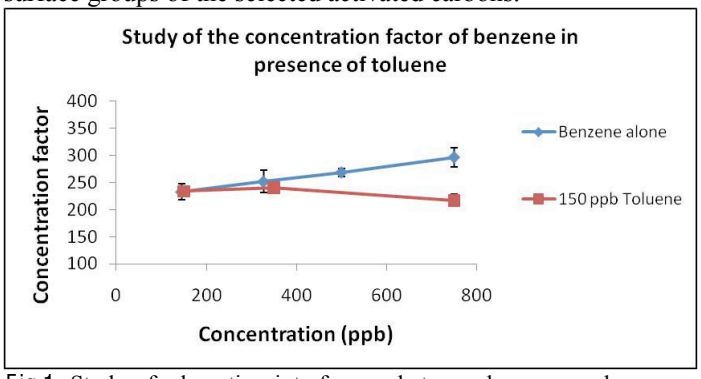

Fig.1. Study of adsorption interference between benzene and toluene

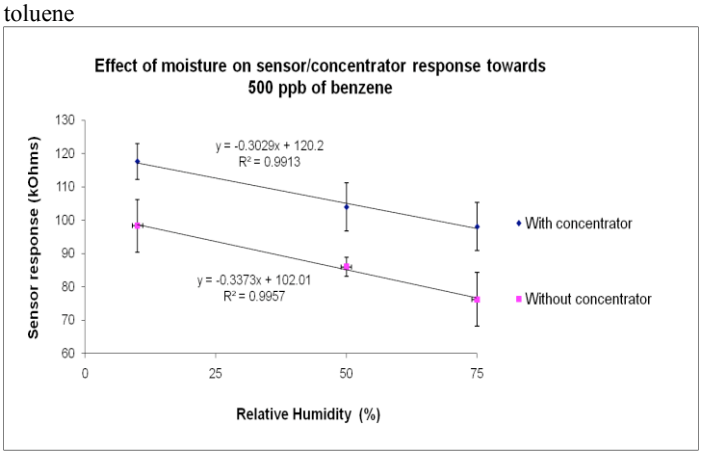

Fig.2. Study of humidity effect on benzene preconcentration

4. Conclusion

A planar microfabricated preconcentrator with high heated area and low power consumption was fabricated. Thanks to the performance of activated carbon, to the well developped active area offered by the designed pre-concentrator, and to the optimization of its preconcentration conditions, concentration factors as high as 200 have been achieved, with a narrow desorption pulse towards benzene, especially when a planar structure is used. Also, the preconcentrator was shown to be unaffected by humidity, which is an excellent result that confirms the applicability of this preconcentrator in real applications where air humidity may vary.

References (Times 10 bold)

[1] Carcinogenic effects of benzene: Update, 1998; EPA/60/p-97/001 U.S., Environmental Protection Agency, U.S. Government Printing Office: Washington, DC.
[2] I. Voiculescu et al., Trends in Analytical Chemistry 27 (4) (2008) 327–343.
[3] S.A. Casalnuovo et al., Eur. Frequency Time Forum, 1999, IEEE Int. Frequency Control Symp., Proc. 1999 Joint Meeting, Besançon, France, 1999, pp. 991–996.
[4] R. Inglés et al., Sensors and Actuators A: Phys. (2011), in press: doi:10.1016/j.sna.2011.03.025.
[5] H. Lahlou et al., Sensors and Actuators B: Chem. (2010), in press: doi:10.1016/j.snb.2009.12.040.

Electrical properties of Eu^{3+}:La_2O_3/P3HT nanocomposites characterized by current-sensing atomic force microscopy

M. Méndez[1,2,3], L.F. Marsal[1*], J.J. Carvajal[2], Y. Cesteros[3], P. Formentín[1], J. Pallarès[1], P. Salagre[3], M. Aguiló[2], F. Díaz[2]

[1] NePhoS-EMaS, Dept. d'Enginyeria Electrònica, Univ. Rovira i Virgili (URV), Campus Sescelades, Avda. Països Catalans, 26, E-43007 Tarragona, Spain

[2] FiCMA-FiCNA-EMaS, Dept. de Química Física i Inorgànica, Univ. Rovira i Virgili (URV), Campus Sescelades, Marcel·lí Domingo, s/n, E-43007 Tarragona, Spain

[3] GreenCat-EMaS, Dept. de Química Física i Inorgànica, Univ. Rovira i Virgili (URV), Campus Sescelades, Marcel·lí Domingo, s/n, E-43007 Tarragona, Spain

**e-mail: lluis.marsal@urv.cat*

Abstract

New hybrid nanocomposites were successfully fabricated by spin coating technique onto ITO-coated glass substrates. Europium doped lanthanum oxide nanocrystals were embedded into poly(3-hexylthiophene) (P3HT) organic films owing to their raising of interest in solar cells and their low quantum efficiency in comparison with silicon solar cells. Thus, Eu^{3+}:La_2O_3 synthesized by sol-gel modified Pechini method were used as a down-shifting material in P3HT organic matrices with the aim of giving the perfect conditions to convert the light emitted from the nanoparticles (NPs) on energy in the solar cell. As the dimension of devices gets smaller, the change in electrical properties and its measurements on a nanometer scale become increasingly important, because of this the nanocomposites were characterized by current-sensing atomic force microscopy (CS-AFM) technique.

1. Introduction

Due to the ease processing, mechanical, and size advantages, as well as a great spectral range of conjugated polymers, make these materials very attractive for use as active components for solar cells [1], efficient light emitting diodes (LEDs), and other solid state electronic devices.

Down-shifting phosphors have the unique property of absorbing light at wavelengths in the UV and re-emitting light in the visible region, which can be tailored by the rare-earth dopant incorporated into the oxide matrix (such as La_2O_3, Y_2O_3, Lu_2O_3, etc.). In previous works we already study the down-shifting properties of the Eu^{3+}:La_2O_3 nanoparticles (NPs). We dispersed them in the P3HT polymer and demonstrated that it is a suitable matrix that absorbs efficiently the light emitted from the nanocrystals [2].

In this work, we describe the fabrication of the metal-molecule-metal junctions (MMMJs), which corresponds to regioregular poly (3-hexylthiophene 2,5-diyl) (P3HT) and P3HT:Eu^{3+} doped lanthanum oxide (Eu^{3+}:La_2O_3) nanocomposites sandwiched between platinum and indium tin oxide (ITO) electrodes. Furthermore, we try to understand the charge and energy transport of these nanocomposites from the CS-AFM measurements with the aim to study the electrical effects of the Eu:La_2O_3 nanocrystals embedded in the P3HT thin layer.

2. Experimental Part

On the one hand, the La_2O_3 nanocrystals doped with 5 mol % Eu^{3+} were synthesized by the sol-gel modified Pechini method [3]. Several techniques such as X-ray powder diffraction, Raman scattering, Transmission and Scattering electron microscopy, and Photoluminescence and Cathodoluminescence were already used to characterize these NPs [3]. On the other hand, P3HT polymeric powder and P3HT polymeric powder with different amounts of NPs, were stirred overnight to ensure complete dissolution of the powders and good dispersion of the NPs in the polymeric solution. The organic and hybrid films were prepared by spin coating these solutions onto pre-cleaned ITO-coated glass substrates, yielding a film thickness of approximately 100 nm as measured by AFM. Spin coating conditions were 2000 rpm, 50 Ac for 1 min and adding 0,2 ml of polymeric solution on the ITO-coated glass substrates. The devices fabricated were: P3HT (1):(*0*) NPs, P3HT(1):(*0.1*) NPs, P3HT(1):(*0.35*) NPs, P3HT(1):(*0.65*) NPs, and P3HT(1):(*0.8*) NPs. Figure 1 shows a simplified diagram of the CS-AFM setup for

P3HT/P3HT+Eu^{3+}:La_2O_3 samples.

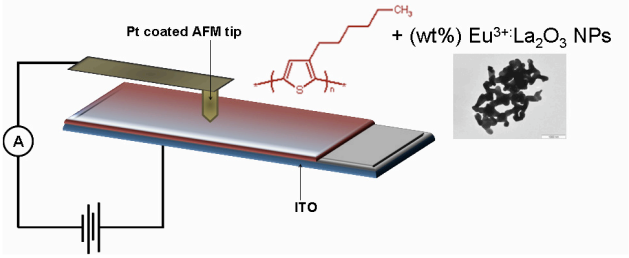

Fig 1. Simplified diagram of the CS-AFM setup for P3HT/P3HT+Eu^{3+}:La_2O_3 samples.

2. Results and discussion

Figure 2 shows the characteristics of the current (I) versus voltage (V) of Pt/P3HT/ITO and Pt/P3HT:(wt%)Eu:La_2O_3/Pt (wt%=10,35,65, and 80%) devices. The asymmetrical nature of the curves is attributed to the difference in the work function of the electrodes, implying different barriers at each electrode/polymer interface ($\Phi_{Pt} > \Phi_{ITO}$).

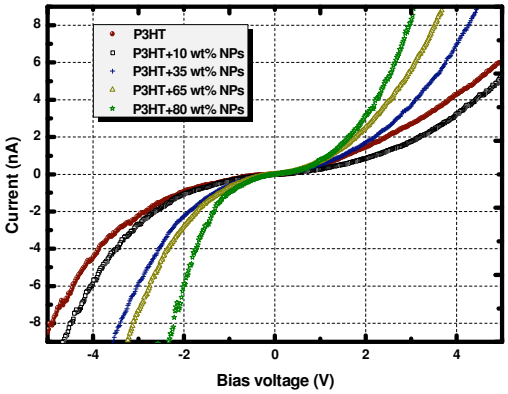

Fig 2. Current-voltage curves of Pt/P3HT/ITO, Pt/P3HT:(wt%)Eu:La_2O_3/ITO (wt=10,35,65,80%).

Furthermore, the different devices showed different I-V curves. The devices raised at a lower voltage when the weight percentage of Eu:La_2O_3 NPs was higher. These differences between them can be associated to a thinner polymer film due to the higher weight percentage of NPs. In fact, when we increase the wt% NPs, we are decreasing the wt% of P3HT of the device. The thickness of the devices was then obtained by scrapping off part of the thin film, and using the AFM in tapping work mode. The thickness were 100,115,97,75,60 nm for P3HT, P3HT+10% wt% NPs, P3HT+35% wt% NPs, P3HT+65% wt% NPs, and P3HT+80% wt% NPs, respectively. The thickness almost totally agreed with the I-V curves, unless the thickness taken for the P3HT and P3HT+10 wt% NPs. This can be considered as a lack of reproducibility in the spin coating technique and also attributed to the way to measure the thickness.

Fowler-Nordheim (FN) plots were used to estimate the position of the molecular orbital closest to the Fermi level. However, by performing transition voltage spectroscopy (TVS), technique which has been established recently, it was possible to directly determine the identity of the closest molecular orbital. All the curves exhibited a clear minimum (see Fig. 3), called as the transition voltage (V_{trans}), which is expected to indicate, approximately, the energetic separation between the Fermi level and the closest molecular orbital. The results of the V_{trans} for the reverse case were 1.98, 2.11, 2.07, 1.61, and 1.1 V for ITO/P3HT/Pt, ITO/P3HT+10wt%NPs/Pt, ITO/P3HT+35wt%NPs/Pt, ITO/P3HT+65wt%NPs/Pt, and ITO/P3HT+80wt%NPs/Pt, respectively.

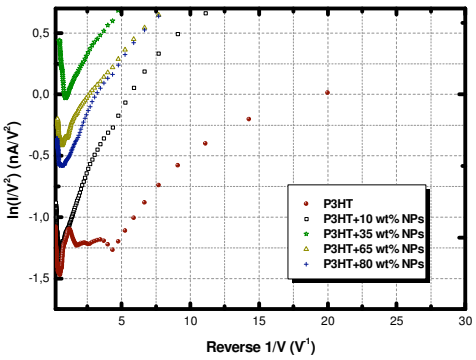

Fig 3. Fowler-Nordheim plot for the tunnelling of holes from Pt into P3HT:(wt%)Eu:La_2O_3.

The results were in agreement with the different height barrier, which needs to be broken by the charge transport mechanisms.

3. Conclusions

Nanocomposites have been successfully fabricated by spin-coating technique and have been characterized by CS-AFM. Furthermore we have demonstrated that the measurement of V_{trans} for a molecular junction can be used as a direct probe of charge transport in molecular systems. Furthermore, the thickness of the thin polymeric layer plays an important role in the I-V curves, as expected and we attributed the different intensities in the current to the thickness of the different fabricated devices. We have also demonstrated the good coexistence of organic and inorganic materials.

Acknowledgements

This work was supported by the projects MAT2008-06729-C02-02/NAN, TEC2009-09551, TEC2010-21574-C02-02, CSD2007-00007, AECID-A/024560/09, PI09/90527, DE2009-0002, 2009SGR1238, 2009SGR549, 2009SGR235; and the Research Center on Engineering of Materials and Systems (EMaS). J.J.C. is supported by the Research and Innovation Ministry of Spain and European Social Fund under the Ramón y Cajal program, RYC2006-858.

References

[1] S.S. Bavel, M. Bärenklau, G. With, H. Hoppe, J. Loos, Adv. Funct. Mater. pp. 1458, 20, 2002.

[2] M. Méndez, Y. Cesteros, L.F. Marsal, E Martínez-Ferrero, P. Salagre, P. Formentín, J. Pallarès, M. Aguiló, F. Díaz, J.J. Carvajal, Opt. Mater. pp. 1120, 33, 2010.

[3] M. Méndez, J.J. Carvajal, Y. Cesteros, M. Aguiló, F. Díaz, A. Guiguere, D. Drouin, E. Martínez-Ferrero, P. Salagre, P. Formentín, J. Pallarès, L.F. Marsal, Opt. Mater. pp. 1686, 32, 2010.

Determination of the band offsets and charges concentrations from capacitance vs voltage characteristics in Pentacene/C_{60} Solar Cells

J.C. Nolasco,[1] Antonio Sánchez-Díaz,[2] R. Cabré,1 J.Ferré-Borrull, [1] L.F. Marsal,[1] E. Palomares, [2,3] J. Pallarès[1]

[1]Departament d'Enginyeria Electrònica Elèctrica i Automàtica, Universitat Rovira i Virgili,Avda. Paisos Catalans 26, 43007 Tarragona, Spain; * E-mail: josep.pallares@urv.cat

[2]Institute of Chemical Research of Catalonia (ICIQ). Avda. Països Catalans, 16 Tarragona 43007, Spain; E-mail: e.palomares@iciq.es

[3]Institució Catalana de Recerca i Estudis Avançats (ICREA), Passeig Lluís Companys, 23 08010 Barcelona,Spain.

1. Introduction

Previously it was claimed that by tailoring the band offsets for electron ΔEc and hole transfer ΔEv, it is possible to increase the open circuit voltage Voc in organic solar cells. [1]. More recently it was proposed that the effective doping density, which is related to the Fermi level, of the active layers also are related to the Voc [2]. Actually we do not find studies to calculated the charge concentration in dark for both active materials into the solar cell structure, neither to calculated the band diagram in thermal equilibrium. This band diagram is useful to support the electrical transport and to calculated some physical parameters like band offsets, built in potential, electron affinities, and interface barriers among others parameters.[3,4]. In this work we point out the calculation of the effective doping density for both active materials and the band offsets using the capacitance voltage measurements C-V and a band diagram in thermal equilibrium calculated with the semiconductor simulator AFORS-HET.

2. Results and Discussions

Fig. 1 shows the $1/C^2$ versus V dependence experimental curve on voltage profile. It consist of two regions (I and II), related to charge concentration variation of the space charge region in every side of the heterojuntion. Assuming that the C60 is the layer with the lowest doping concentration, the effective doping density and therefore Fermi level d1 = 0.18eV,and built in voltage Vd = 0.97 eV were calculated from the profile of region II, These values were calculated using the well know Mott-Shottky relationship. On the other hand, the Fermi level of Pentacene d2 = 0.11 eV, was calculated from the slope of region I, using Chopra and Das model [5] assuming that the layer which lowest effective doping density (C60) is totally depleted. The assumptions were proved through a comparation between the simulation of the capacitance voltage curve (line in Fig. 1) and the experimental one (symbols in Fig. 1).

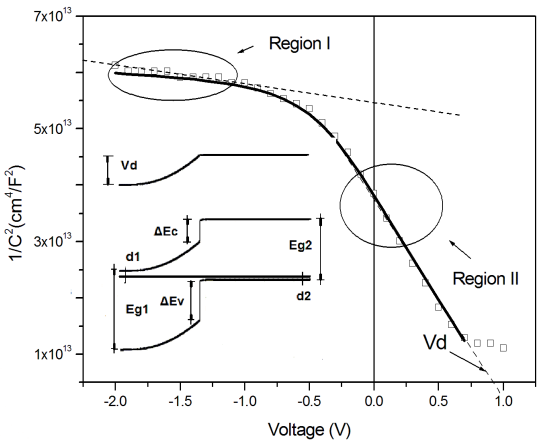

Fig.1 Simulated (line) and experimental (symbols) $1/C^2$ versus voltage curve and band diagram (inset) of Pentacene/C60 solar cell.

From the calculated band diagram model, the band offset ΔEc and ΔEv are given as follow: ΔEc = Eg2-d2-d1-Vd and ΔEv = Eg1-d2-d1-Vd. Where Eg2 and Eg1, are the band gap of Pentacene and C60 respectively. From the literature Eg2 = 2.05 eV and Eg1 = 2.67 eV

[6]. The band offset calculated values are : $\Delta Ec = 0.79$ eV and $\Delta Ev = 1.40$ eV, which are similar to: 0.70 eV and 1.32 eV respectively calculated from the difference between HOMO's and LUMO's energy values [6].

3. ACKNOWLEDGMENT

This work has been supported by the Spanish Ministry of Science under project number TEC2006-06531, TEC2009-09551 and HOPE CSD2007-00007 (Consolider-Ingenio 2010).

4. REFERENCES

[1] Barry P. Rand, Diana P. Burk, Stephen R. Forrest, Phys. Rev B 75, 115327 (2007).
[2] R. A. Street, M. Schoendorf, A. Roy and J. H. Lee. Phys. Rev. B 81, 205307 (2010).
[3] J. C. Nolasco, R. Cabre, J. Ferre-Borrull, L. F. Marsal, M.Estrada and J. Pallares J. Appl. Phys. 107, 04455 (2010).
[4] J. C. Nolasco, AntonioSanchez-Diaz, R. Cabre, J. Ferre-Borrull, L. F. Marsal and J. Pallares, Appl. Phys. Lett. 97, 013305 (2010).
[5] Chopra K. L. and DAS S. R. (1983). In Thin Film Solar Cells, pp. 7-12, Plenum Press, New York and London.
[6] Peter I. Djurovich, Elizabeth I. Mayo, Stephen R. Forrest, Mark E. Thompson, Organic Electronics 10 515 (2009).

A Compact Double-Gate MOSFET Model Consistent with a Multi-Subband Ensemble Monte Carlo Model

[1]M. Cheralathan, [2]C. Sampedro, [2]J.B. Roldán, [2]F. Gámiz and [1]B. Iñiguez

[1]DEEEA, Universitat Rovira i Virgili (URV), Tarragona 43007, Spain E-mail: muthupandian.cheralathan@urv.cat.
[2]Nanoelectronics Research Group, Dept Electronics. University of Granada. 18071 Granada, Spain.

1. Abstract

In this paper we extend a Double Gate (DG) MOSFET model to nanometer technology nodes in order to include the hydrodynamic and quantum mechanical effects, and we show that the final model can accurately reproduce Multi-Subband Ensemble Monte Carlo Simulations. Template devices representative of 22nm and 16nm DG MOSFETs were used to validate the model. The final model includes the main short-channel and nanoscale effects, such as mobility degradation, channel length modulation, drain-induced barrier lowering, overshoot velocity effects and quantum mechanical effects.

2. Introduction

Ultra-thin-film body MOS transistors and, in particular, double-gate (DG) MOSFETs are considered to be a very attractive option to improve the performance of CMOS devices. Nanoscale DG-MOSFETs introduce challenges to compact modeling associated with the enhanced coupling between the channels, ballistic or quasi-ballistic transport, quantum confinement, etc. In this work we present the extension of a DG MOSFET model to nanoscale technology nodes by incorporating quantum mechanical and hydrodynamic transport effects validating it by comparison with Monte Carlo (MC) simulations. Our starting point in this paper is a classical analytical model for the undoped DG-MOSFET [1] based on a unified charge control model [2]. The final compact model for the drain-current includes mobility degradation, short-channel effects (SCE), or channel length modulation (CLM). Velocity overshoot is also modeled through the hydrodynamic transport and quantum effects are extended from the classical compact model [3]. The results of the comparison between the compact model and MC simulations are presented and discussed in this work.

3. Simulation Approaches

The advanced modeling approach used for the calibration of the compact model is based on the direct solution of the Boltzmann-Transport-Equation (BTE) using the Monte Carlo method. In particular, the Multi-Subband Ensemble Monte Carlo (MSB-EMC) simulator has been used [4]. This method is based on the mode-space approach of quantum transport. The Monte Carlo family model incorporates all relevant scattering mechanisms such as surface roughness (SR), acoustic and phonon scattering. We have accurately modeled these MC simulations using our compact model (with physical parameter values), taking into account the physical mechanisms included in their approach. The drain current expression is based on a unified charge control model which is written in terms of charge densities at the source and drain ends. This drain current expression includes the hydrodynamic transport model. Velocity overshoot is included in the model using a one dimensional energy-balance model [5]. We have included a correction in the oxide capacitance using the inversion-layer centroid [6] to take into account the quantum mechanical effects. The low-field mobility data are obtained from a model that takes into account the mobility degradation [7] due to quantum effects. We have also included the effects of channel length modulation (CLM) and drain-induced barrier lowering (DIBL). The quantum confinement correction is included in the model that makes a positive shift in the threshold voltage of the device (n-channel) [8].

4. Results and Discussions

Fig. 1 and 2 shows the transfer characteristics for 22 nm and 16 nm DG-MOSFETs, respectively. A good agreement between the compact model and the MSB-EMC simulations is obtained. In particular, the mobility degradation is well reproduced. Fig. 3 shows the output characteristics of the 22 nm (top) and 16 nm (bottom) DG MOSFETs. A good agreement between the compact model and the MSB-EMC simulations are seen. It can be seen that the model without the effect of velocity overshoot and quantum effects, a good agreement is obtained at low drain bias and becomes lower at higher drain bias. If the quantum effects are not included in the model, the current is significantly higher than the MC simulations. If the hydrodynamic transport is not considered the model gives much lower current values than the simulation. It can be inferred that the hydrodynamic model can be used to compare results from advanced transport models such as MSB-EMC simulations.

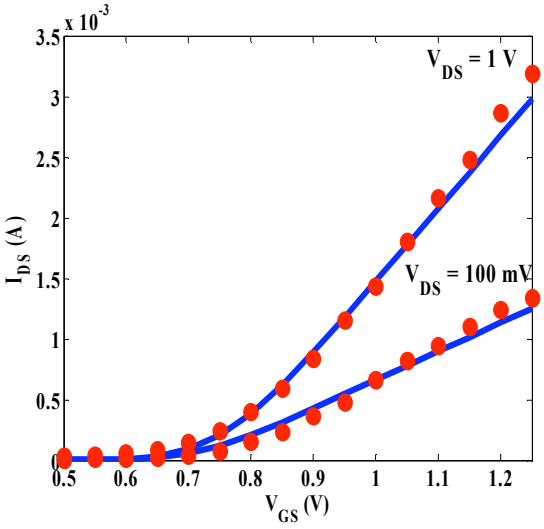

Fig.1: *Trans-characteristics of 22 nm DG-MOSFET for low and high V_{DS} Solid lines: Compact model, Symbols: Simulations (UGR MSB-EMC).*

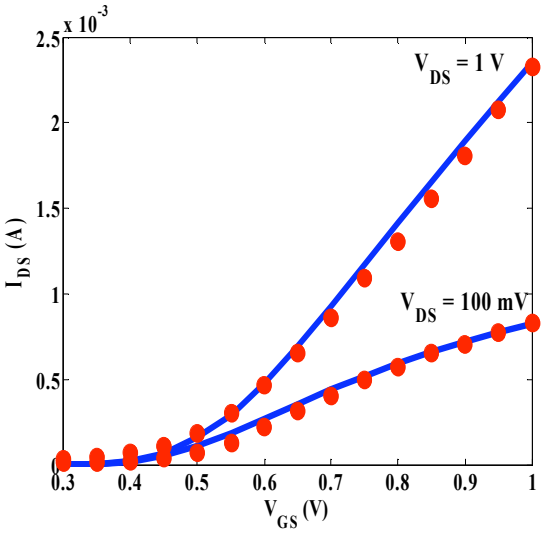

Fig.2: *Trans-characteristics of 16 nm DG-MOSFET for low and high V_{DS} Solid lines: Compact model, Symbols: Simulations (UGR MSB-EMC)*

5. Conclusions

The comparison between the advanced modeling approach and the compact model for the drain current in nanoscale DG MOSFETs are presented. We present a compact DG MOSFET model to reproduce results obtained from the Multi-Subband Ensemble Monte Carlo simulator for the 22 nm and 16 nm technology nodes. The model is valid and continuous through all operating regimes. Nanoscale and short-channel effects are taken into account, including velocity overshoot and quantum mechanical effects. The model shows a very good agreement with the MC simulations for the practical range of voltages considered.

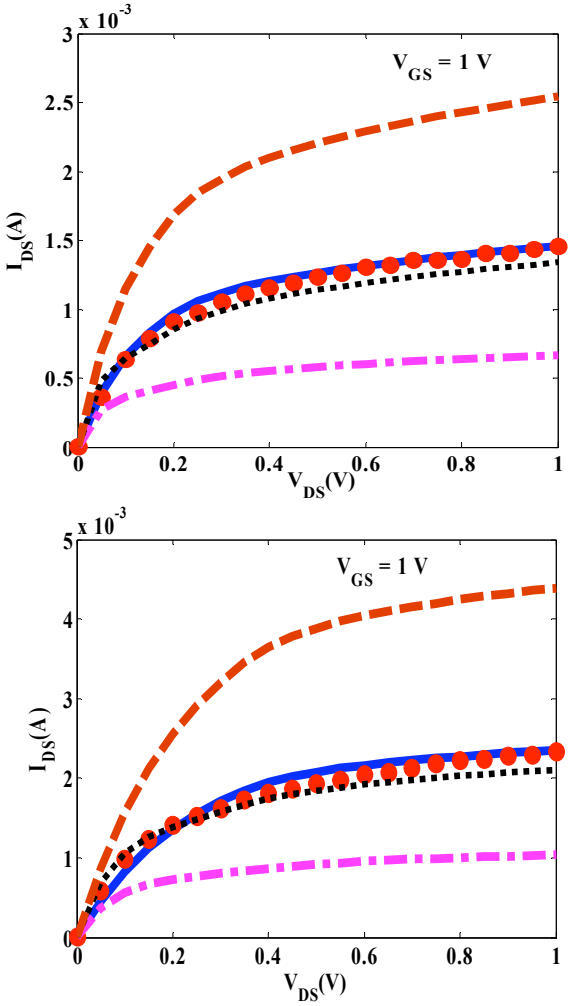

Fig.3: *Output characteristics of the 22 nm (top) and 16 nm (bottom) DG-MOSFET for V_{GS}=1V Dashed line: Without quantum effects, Solid line: Compact model, Dotted line: Without velocity overshoot and quantum effects, Dash-dotted line: Without hydrodynamic transport, Symbol: Simulation (UGR-MSB-EMC).*

Acknowledgements

Work supported by the MICINN (Spanish Government) under Project TEC2008-06758-C02-02, by the UE under contracts 216171 "NANOSIL", 218255-"COMON" and 216373 "EUROSOI", by the ICREA Academia Award and by the PGIR grant (URV).

References

[1] F. Lime et al. IEEE Trans.Electron Devices, vol. 55, no. 6, pp. 1441-1448, Jun. 2008.
[2] J.-M. Sallese et al. Solid State Electron., vol. 49, no. 3, pp. 485-489, Mar. 2004.
[3] O. Moldovan et al. IEEE Trans.Electron Devices, vol.57, no.7, pp. 1718-1724, Jul. 2007.
[4] C. Sampedro et al. Sol. State Elec., 54 (2010) 131-136.
[5] A. Lázaro et al. Journal of Applied physics, 100, 084320-12, 2006.
[6] J.A. López-Villanueva et al. IEEE Trans.Electron Devices, vol. 47, no. 1, pp. 141-146, Jan 2000.
[7] G.Baccarani et al. IEEE Trans.Electron Devices, vol. 46, no. 8, pp. 1656-1666, Aug. 1999.
[8] M. Tang et al. IEEE Trans. Electron Devices, vol. 56, no. 7, pp. 1543-1547, Jul. 2009.

Transformation of Nanoporous Anodic Alumina pattern on Si substrate

Mohammad Mahbubur Rahman, Josep Ferré-Borrull, Abel Santos, Pilar Formentín, Josep Pallarès, Lluis F. Marsal

josep.ferre@urv.cat
NePhoS, Nano-electronic and Photonic Systems, DEEEA,
Universitat Rovira i Virgili, Av. Paisos Catalans 26, 43007, Tarragona, Spain

Abstract

Nano porous anodic alumina shows photonic properties such the existence of a stop band [1]. In this work, self-assembled porous anodic alumina on silicon substrates are fabricated with the aim to transfer the pattern to the Si. Such pattern will be obtained by the wet chemical etching using TMAH. One of the main goals of this investigation is to obtain of nanostructured porous silicon for optical characterization and demonstration of the photonic properties of the porous anodic alumina structure. Thus, special attention will be paid to the achievement of a good surface quality of the final nanostructured Si.

1. Introduction

Porous silicon (Si) based semiconducting materials with certain degree of ordered nanostructures have generated considerable interest in both basic research and commercial applications because of their electronic, optical or magnetic characteristics [2-3]. Conventional lithographic technique using optical, electron, or x-ray beams are used for the fabrication of porous Si. An inexpensive technique called the natural lithography, which is based on a self-organization process, has recently attracted increasing attention because it can be the key method for the nanofabrication due to its relative simplicity and low cost. Several studies have been reported on the nanopatterning of semiconductors using self-assembled colloidal particles [3-5] or self-ordered anodic porous alumina [6-8].

In this communication we will report on the investigation of the porous silicon and nanoporous anodic alumina (NAA) structures. The NAA is a self-assembled porous material with a 2D pattern having characteristic interpore distance over the wavelength of visible light [9, 10]. We will report the method of the fabrication of NAA-based quasi-random structures on silicon (Si) substrate that can be used as a lithographic mask for obtaining porous Si by electrochemical etching. The NAA pattern on Si substrate was transferred by wet chemical etching using TMAH [11]. After complete removal of the NAA layer from the Si substrate the porous Si was observed in AFM. As we are aiming to obtain the porous Si for optical characterization and demonstration of the photonic properties of the NAA structure, so we have to pay attention to achieve a good surface quality of the final nanostructured Si.

2. Method of Fabrication

An aluminum film of thickness 1.5 µm was sputtered on a p-type Si substrate (1–5Ωcm and <100> crystal orientation). The sputtering power was 200W, and the deposition rate was about 1 Å/s. An Ohomic contact was made between the bottom of the Si substrate and the Al film using silver glue. The two-step anodization method was followed. The first step was performed for 7 minutes at a constant voltage of 40 V in 0.3 M dm^{-3} oxalic acid at room temperature. The oxide film formed in this first step was completely removed by immersing the specimens in a mixture of phosphoric acid and chromic acid. The second step was performed under the same anodization conditions as the first step. The formation behavior of anodic porous alumina on the Si substrate was examined by measuring current density transient at a constant voltage and the process was stopped when the current density reaches the minimum value. To remove the barrier layer from the bottom of the pore, the sample was immersed in 5% weight H_3PO_4 at 35˚C for 16 minutes. The transformation of the pattern has been performed by immersing the sample in 4% wt TMAH solution for 8 minutes at 37˚C.

3. Results and Discussions

Figs. 1(a) and (b) show the current transient of the first

and the second step of the anodization respectively. The saturation stage of the second step shown in fig. 1(b), indicates the progress of the anodization. The current remains steady during the anodization process indicating the homogeneity of the sputtered aluminum film on the Si substrate. The anodization process was stopped when the current reaches its minimum indicating the complete consumption of Al sputtered on Si substrate. Overanodization accompanied by extensive gas evolution is not suitable for the appliance of anodic porous alumina to mask as it causes the local destruction of the porous film [12]. To be able to transfer the pattern on Si it is necessary to remove the barrier layer by immersing in phosphoric acid at 35˚C for 16 minutes. After the selective removal of the barrier layer, wet chemical etching by TMAH was started.

After electrochemical etching through NAA, the geometric pattern on the Si substrate was observed by AFM shown in figure 2. The size of the pores and the periodicity in Si depending on the NAA that is approximately 100 nm for the formation voltage of 40 V. This result indicates that the porous pattern of Al has been transferred to Si substrate. Since we are aiming to use this porous structure for the optical characterization and demonstration of the photonic properties of the NAA structure, thus, special attention will be paid to achieve of a good surface quality of the final nanostructured Si.

4. Conclusions

In this work we have shown the first results achieved in our lab on the transfer of the nanoporous anodic alumina quasi-random structure to a conductive substrate such as silicon. The steady value of the current transient indicating that the Al sputtered on Si substrate is homogeneous and good control over the anodization process ensures the appropriate point to stop the process. The transformation of the porous pattern from NAA onto Si substrate using TMAH has been studied. Although we succeed to transfer the pattern, further improvement is required to obtain good surface quality and high aspect ratio of the nanopore array that can be done by improving etching conditions, using different types of electrolytes, electrolyte temperature, current density, substrate parameters, resistivity, doping density etc.

5. References:

1. Mohammad Mahbubur Rahman, Josep Ferré-Borrull, Josep Pallarès, and Lluis F. Marsal, Phys. Status Solidi C 8, No. 3, 1066–1070 (2011).
2. A. G. Cullis, L. T. Canham and P. D. J. Calcott, J. Appl. Phys. 82 (3), (1997).
3. Laiho, R., Journal of Luminescence, vol. 57, issue 1-6, pp. 197-200.
4. H. W. Deckman and J. H. Dunsmuir, Appl. Phys. Lett. 41,377 (1982).
5. C. Haginoya, M. Ishibashi, and K. Koike, Appl. Phys. Lett. 71, 2934 (1997).
6. Y. Lu, S. Theppakuttai, and S. C. Chen, Appl. Phys. Lett. 82, 4143 (2003).
7. H. Masuda and M. Satoh, Jpn. J. Appl. Phys. 35, L126 (1996).
8. M. Nakao, S. Oku, T. Tamamura, K. Yasui, and H. Masuda, Jpn. J. Appl.Phys. 38, 1052 (1999).
9. Y. Kanamori, K. Hane, H. Sai, and H. Yugami, Appl. Phys. Lett. 78,142 (2001.
10. A. P. Li, F. Müller, A. Birner, K. Nielsch, and U. Gösele, J. Appl. Phys. 84, 6023 (1998).
11. L. Vojkuvka, L. F. Marsal, J. Ferre-Borrull, P. Formentin, and J. Pallares, Superlattices Microstruct. 44, 577 (2008).
12. Thompson, G. E., Furneaux, R. C., Wood, G. C., Richardson, J. A. & Goode, J. S. *Nature* **272**, 433–435 (1978).

6. Acknowledgements

This work was supported by Spanish Ministry of Ciencia e Innovacion (MICINN) under grant number TEC2009-09551, HOPE CSD2007-00007 (Consolider-Ingenio 2010) and AECID-A/024560/09

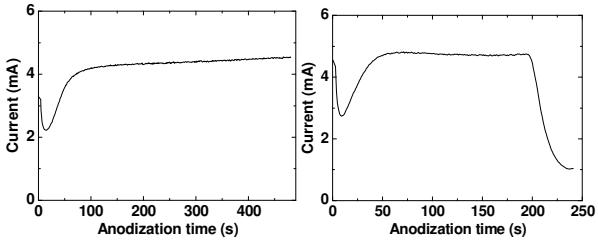

(a) (b)

FIG.1. Anodization time-current curve of the aluminum film sputtered on Si in 0.3 M dm^{-3}oxalic acid at 20 °C at 40 V. The fig. 1. (a) and 1.(b) shows the first step and the second step of anodization respectively.

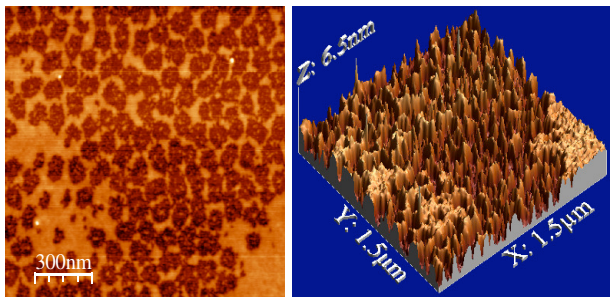

(a) (b)

FIG.2. AFM image of the patterned Si after chemical etching in TMAH solution. The fig.2(a) AFM tapping-mode image of the surface of silicon and (b) the three dimensional image of the same surface.

.

Vital Signs Monitoring using Impulse Based UWB Signal

A. Lázaro, D. Girbau, R. Villarino, A. Ramos[1]

Department of Electronic, Electric and Automatic Engineering, Escola Tecnica Superior d'Enginyeria, Universitat Rovira i Virgili. Av. Països Catalans 26, 43007 Tarragona, Spain.
[1] angel.ramos@urv.cat

Non-contact monitoring of vital signs has been achieved by Doppler radars since several years ago [1-3], with accurate results. There are interesting applications with these systems, such as cardiopulmonary monitoring for sleep apnea syndrome, preventing the sudden infant death syndrome, and finding human subjects trapped in earthquake rubble.

Ultra-Wideband (UWB) technology uses sub-nanosecond pulses instead of narrow-band carriers. It has become a promising alternative to existing Doppler radars because it consumes less power, coexists well with other instruments, and is robust to interference and multipath [4-6].

This work presents a measurement setup based on a UWB radar to detect vital signs. Also, to improve the quality of the signals, two processing techniques are introduced. The first one is an harmonic canceller implemented with a filter based on the Moving Target Indicator. The second is a body movement compensation technique.

We will use the UWB radar by Geozondas described in [6], that is, a pulse generator, which transmits a UWB pulse to the test subject, and a sampler converter in the receiving chain. Also, two different antennas will be used: a bow tie antenna with a plane reflector (antenna 1) and a tappered slot Vivaldi antenna (antenna 2).

The received pulse will vary its time-of-arrival (ToA) and it will be a periodic function of the chest displacement due to respiration and heart movements. Using the model in [6], we can represent the received signal r as a sum of normalized pulses p:

$$r(t,\tau) = \sum_i A_i\, p(\tau - \tau_i) + Ap(\tau - \tau_d(t)) \qquad (1)$$

where i accounts for each multipath component, being A_i and τ_i its amplitude and pulse delay, respectively. The other part of (1) accounts for the desired signal, being A the amplitude of the pulse reflected on the body, and $\tau_d(t) = 2d(t)/c$:

$$d(t) = d_0 + m(t) = d_0 + m_b \sin(2\pi f_b t) + m_h \sin(2\pi f_h t) \qquad (2)$$

where d_0 is the nominal distance around $d(t)$ changes, c is the light velocity, and m_b and m_h are the respiration and heartbeat displacement amplitudes, and f_b and f_h are the respiration and heartbeat frequencies, respectively. The received waveforms are measured at discrete instants in slow time t, sampled at a fast time τ.

We can remove the background clutter by substracting the average of all received waveforms from the original signal, becoming x:

$$x(t,\tau) = r(t,\tau) - \lim_{T\to\infty}\frac{1}{T}\int_0^T r(t,\tau)dt = Ap(\tau - \tau_d(t)) - r_0(\tau) \qquad (3)$$

Finally, we can remove the DC component $r_0(t)$ by substracting the average of all samples in fast-time, becoming y:

$$y(t,\tau) = x(t,\tau) - x_0(\tau) = Ap(\tau - \tau_d(t)) \qquad (4)$$

To compensate random body movements, such as the ones done by the operator of the radar or by the very person being monitored, we present the following solution. We use the first waveform as reference, and cross-correlate the reference with the next waveforms. The delay position of the peak of cross correlation is used to shift each waveform and align all of them, compensating the delay due to body movement. The resulting Fourier Transform slow-time is:

$$Y(f,\tau_0) = A\sum_{k=-\infty}^{+\infty}\sum_{l=-\infty}^{+\infty} C_{kl}\,\delta(f - kf_b - lf_h) \qquad (5)$$

$$C_{kl} = \int_{-\infty}^{+\infty} P(\nu)J_k(\beta_b\nu)J_l(\beta_h\nu)d\nu \qquad (6)$$

where $\beta_b = 4\pi m_b/c$ and $\beta_h = 4\pi m_h/c$, and τ_0 correspond to the delay for the maximum amplitude of the received pulse. The spectrum in (5) consists of a train of delta functions centered at the frequencies of the harmonics

of f_b, f_h and their intermodulation products. The amplitude of each delta is controlled by the coefficient C_{kl}. The fundamental component of breathing and hearbeat are C_{10} and C_{01} respectivelly. We can use the Chirp-Z transform (CZT) [6] to determine the breathing and heart beat frequencies. Fig. 1 shows some measured amplitudes depending on breath amplitude for the two antennas used, and Table 1 shows a comparison between Doppler radar in [3] and our UWB radar in frequency detecting for different subject angles, achieving similar results.

To remove harmonics, we also present a harmonic canceller, with a filter based on the Moving Target Indicator (MTI), shown in Fig. 2, which can be repeated several times in cascade.

Fig. 3 shows how the presented techniques, movement compensation and MTI, can improve the measurements. It can be seen that using both not only gives most accurate results but body movement compensation is necessary to ensure the efficiency of MTI filtering. With both techniques, the body signals can be properly detected.

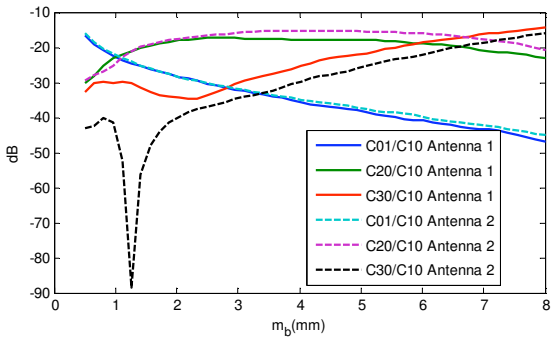

Fig.1. Normalized heartbeat amplitude (C_{01}/C_{10}) and second (C_{20}/C_{10}) and third (C_{30}/C_{10}) harmonics of the breathing as function of breath amplitude mb for antenna 1 and antenna 2.

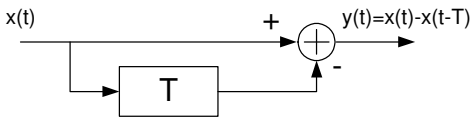

Fig.2. Implementation of a single-delay canceller.

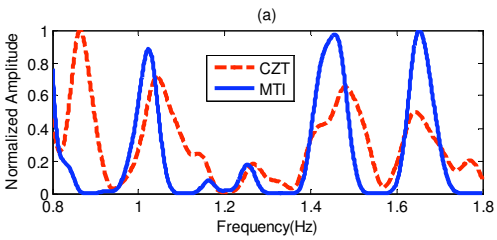

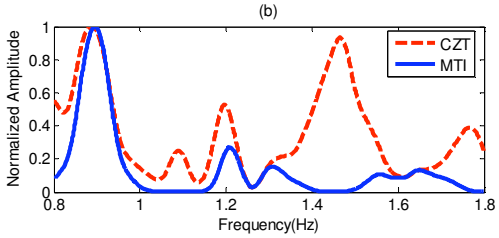

Fig.3. Spectrum of heart signal obtained from Chirp Transform and MTI filtering. (a) without movement compensation and (b) with movement compensation.

Angle	**UWB Radar**					**Doppler Radar**	
(deg)	f_b	f_h	C_{01}	C_{20}	C_{30}	f_b	f_h
0º	25.9	69.9	-25.2	-20.2	-33.1	25.6	68.6
45º	23.6	67.9	-29.4	-12.5	-37.0	24.4	63.0
90º	22.8	80.8	-22.5	-17.0	-20.0	23.3	79.7
135º	22.6	58.3	-10.1	-10.2	-13.5	22.9	54.4
180º	23.1	54.6	-7.4	-9.6	-12.5	23.3	54.1

Table 1. Results as a function of body orientation. Cij represents the normalized harmonic level in dB with respect the respiration component C10, fb and fh are expressed in breathing/min and beats/min, respectively.

References

[1] C.Li, J.Lin, "Complex Signal Demodulation and Random Body Movement Cancellation Techniques for Non-contact Vital Sign Detection," IEEE Int. MTT-S Microwave Sym. Digest 2008, pp.567-570.

[2] B. Park, O. Boric-Lubecke, V.M.Lubecke, "Arctangent demodulation with DC offset compensation in quadrature Doppler radar receiver systems," IEEE Trans. Microwave Theory and Techniques, vol. 55, pp. 1073-1079, May 2007.

[3] D.Girbau, A.Lazaro, A.Ramos, R.Villarino, "Remote sensing of vital signs using a Doppler radar and diversity to overcome null detection", to be published in IEEE Sensors Journal.

[4] S.Venkatesh, C.Anderson, N.V.Rivera, R.M.Buehrer, "Implementation and Analysis of Respiration- Rate Estimation Using Impulse-Based UWB," 2005 IEEE Military Communications Conference (IEEE Milcom '05), October 2005, Vol.5, 3314-3320, 2005.

[5] M.Y.W.Chia, S.W.Leong, C.K.Sim, K.M.Chan, "Through-wall UWB radar operating within FCC's mask for sensing heart beat and breathing rate", IEEE European Microwave Conf. 2005, Vol.3, 1-4, 2005.

[6] A.Lazaro, D.Girbau, R.Villarino, "Analysis Of Vital Signs Monitoring Using An IR-UWB RADAR," Progress In Electromagnetics Research, PIER 100, 265-284, 2010.

2D I-V Model for Lightly Doped SB-DG-MOSFETs

Mike Schwarz[1,2,✠], Thomas Holtij[1,2], Alexander Kloes[1], and Benjamín Iñíguez[2]
[1]Technische Hochschule Mittelhessen, Giessen, Germany
[2]Universitat Rovira i Virgili, Tarragona, Spain
✠mike.schwarz@ei.th-mittelhessen.de

***Abstract*—A new physics-based current model for lightly doped Schottky barrier Double-Gate MOSFETs (SB-DG-MOSFETs) based on 2D analytical solutions is presented. Essential 2D effects on the currents are included in the model and combined with diffusion effects in the channel region. A comparison of the current with TCAD Sentaurus was made for channel lengths down to 22nm.**

***Index Terms*—Analytical closed-form, conformal mapping, device modeling, Double-Gate (DG) MOSFET, Schottky barrier, thermionic emisson, tunneling current**

I. Introduction

Conventional bulk-MOSFETs are approaching the end of the roadmap. Today, the focus for sub-20nm devices is on SOI-type structures [1], [2] - so called DG-MOSFETs, FinFETs and GAA (Gate-all-around) FETs. These alternatives reduce short channel effects [2]. The Schottky barrier (SB) MOSFET is a promising candidate due to its high scalability, good process compability and the low access resistances [3].

In this paper, we present a Schottky barrier Double-Gate MOSFET current model for lightly doped Schottky barrier devices based on the 2D conformal mapping technique [4] for the electrostatic potential [5] and the electric field [6]. The ambipolar behavior is predicted by the superposition of the separately estimated electron and hole currents.

In Fig. 1 the assumed structure of a SB-DG-MOSFET device is shown with coordinates and boundary conditions.

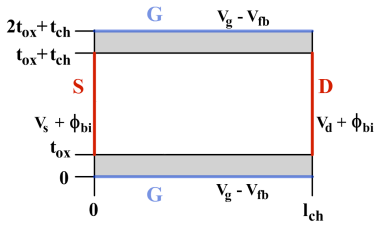

Figure 1. Simplified geometry and boundaries of a SB-DG-MOSFET.

II. Current Calculation

The main contribution of the current in our model result from electrons at the source electrode and holes at the drain electrode depending on the bias condition. It follows

$$I_{TE} = I_{tun} + I_{therm}. \tag{1}$$

The estimation of the tunneling probability is done by using the Wentzel-Kramers-Brillouin (WKB) approximation [7]. Neglecting the Schottky barrier lowering effect, the tunneling probability is calculated via

$$T(\vec{E},x,y) = \exp\left(\frac{-4\sqrt{2m\cdot m_0}\left(|\vec{E}(x,y)|\cdot x\right)^{3/2}}{3q\hbar|\vec{E}(x,y)|}\right). \tag{2}$$

Here m describes the effective mass, m_0 the electron rest mass, q the elementary charge, $\hbar$ the reduced Planck constant and $\vec{E}$ the electric field at the point of interest on the position x (distance from the barrier) and y (Fig. 2) which results from the 2D analytical solution via the conformal mapping technique [5], [6].

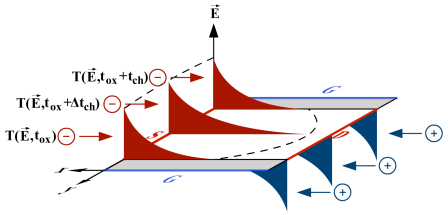

Figure 2. The schematic tunneling probability for inversion mode is calculated depending on the position y.

A. Thermionic Current

The contribution of the thermionic current is predicted as presented in [8]. The current can be expressed as

$$J_{therm}(y) = A^*T^2\exp\left(-\frac{q\phi_B(y)}{kT}\right)\left[1-\exp\left(\frac{-qV_{ds}}{kT}\right)\right]. \tag{3}$$

A^* represents the Richardson constant, $\phi_B(y)$ describes the barrier height or maximum barrier which the charge carriers have to surmount in the slice at position y. For the case of accumulation $\phi_B(y)$ is represented by the minimum of the electrostatic potential in the channel region, calculated by the analytical model in [5]. In inversion $\phi_B(y)$ is obtained by the Schottky barrier height itself.

B. Tunneling Current

With the prediction of (2) and distributions of the charge carriers we are able to calculate the tunneling current density. In contrast to [8], instead of integrating with respect to the energy, here we integrate with respect to coordinate x along the channel

$$J_{tun}(y) = \frac{A^*T}{k}\int_0^{l_{ch}} T(\vec{E},x,y)f_m(\xi(x))\left[1-f_s(\xi(x))\right]\frac{\partial\xi}{\partial x}dx. \tag{4}$$

$T(\vec{E},x,y)$ is the tunneling probability for the carriers. The Fermi-Dirac distributions at the metal/semiconductor contacts are described by $f_m(\xi(x))$ and $f_s(\xi(x))$, where ξ is the charge carrier energy.

C. Drift-Diffusion Effects

The carriers being injected from a barrier by thermionic emission or tunneling will encounter scattering on their way through the channel.

In the following we focus only on electron current from the source. The effect of a drift-diffusion limited current will have an increasing influence if a strong electric field is in the channel near the source barrier which is the case for higher gate biases. The barrier is thinned and tunneling dominates the electron current.

According to the diffusion theory at metal-semiconductor contacts [8] the emission current density from equation (3) can instead be written as

$$J_{therm}(y) = q\mu_n N_C \vec{E}_m \exp\left(-\frac{q\phi_B(y)}{kT}\right)\left[1-\exp\left(\frac{-qV_{ds}}{kT}\right)\right] \quad (5)$$

with carrier mobility μ_n, the effective density of states in the conduction band N_C, and the electric field at the barrier $\vec{E}_m$. This way the tunneling current becomes bias dependent.

In our model we apply this theory to the tunneling current. For this we assume that a carrier, which by tunneling is generated within the conduction band of the channel in distance x to the barrier, will encounter a similar drift-diffusion effect as the carriers considered in equation (5), but with the individual electric field at the position of generation, instead of the field at the barrier. Therefore we can rewrite equation (4) for the tunneling current density:

$$J_{tun}(y) = \frac{q\mu_n N_C}{kT}\int_0^{l_{ch}} |\vec{E}(x,y)|\cdot T(\vec{E},x,y)\cdot f_m(\xi(x))[1-f_s(\xi(x))]\frac{\partial\xi}{\partial x}dx, \quad (6)$$

whereby the total current is obtained by integration over the channel thickness t_{ch} and width w_{ch} and in the subsequent plots is indicated by I_{TE}.

With this result drift-diffusion affects the tunneling current in our model by mobility μ_n. Whereas for thermionic emission current equation (3) is unchanged and is controlled by Richardson's constant. Both parameters are treated as fitting parameters.

III. Results & Discussion

In this section, we show results of our model for various device parameters and biases in comparison with the corresponding numerical device simulations from TCAD Sentaurus [9]. Furthermore, the parameters electron mass m_n, hole mass m_p, mobility μ_n, and Richardson constant A^* have been fitted in the model.

Fig. 3 shows the transfer characteristic in log-scale for a $22nm$ SB-DG-MOSFET at different drain biases, a unique characteristic of SB-DG-MOSFETs. Especially in log-scale we are able to observe the dependency of the hole current from the drain bias V_{ds}. With increasing V_{ds} the hole current increases due to the thinned barrier at the drain junction and the therefore increased probability of the hole charge carriers to tunnel.

Furthermore, a good prediction of the slope to inversion can be observed. In Fig. 4 the corresponding lin-scale plot is shown.

IV. Conclusion

An analytical approach to calculate the current in SB-DG-MOSFETs was presented, which shows a good agreement with the simulation results down to $22nm$ channel lengths. In a new approach we included diffusion theory in the tunneling current calculation. As a result, the model is able to predict the current with ambipolar behavior well for several barrier heights and geometries up to a relatively high gate bias, while our approach in particular inherently includes 2D effects on the device current.

V. Acknowledgment

This project was supported by the German Federal Ministry of Education and Research contract No. 1779X09, by DFG under Grant KL 1042/3-1, by the European Commission under FP7 Projects ICT-216171 ("NANOSIL") and IAPP-218255 ("COMON"), by the Spanish Ministerio de Ciencia y Tecnología under Projects TEC2008-06758-C02-02/TEC, and also by the PGIR/15 Grant from URV and by the ICREA Academia Prize.

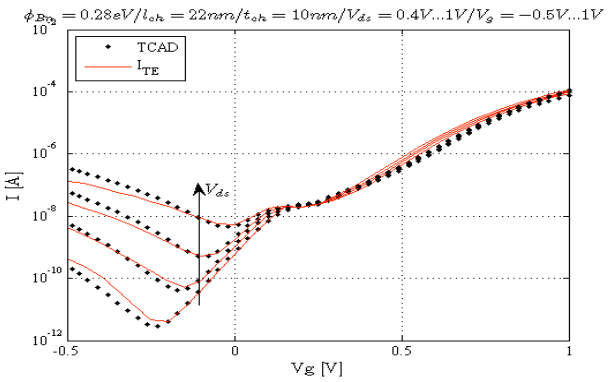

Figure 3. Model for $22nm$ device compared to TCAD (log-scale).

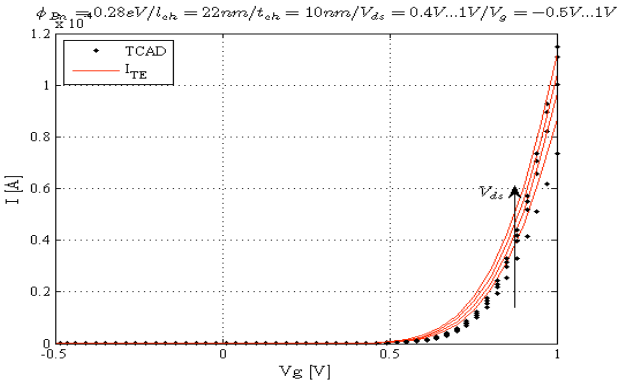

Figure 4. Model for $22nm$ device compared to TCAD (lin-scale).

References

[1] D. Jimenez, B. Iniguez, J. Sune, L. F. Marsal, J. Pallares, J. Roig, and D. Flores, "Continuous analytic I-V model for surrounding-gate MOSFETs." *IEEE Trans. Electron Devices*, vol. 25, no. 8, pp. 571–573, 2004.

[2] N. Collaert, A. De Keersgieter, A. Dixit, I. Ferain, L. S. Lai, D. Lenoble, A. Mercha, A. Nackaerts, B. J. Pawlak, R. Rooyackers, T. Schulz, K. T. Sar, N. J. Son, M. J. H. Van Dal, P. Verheyen, K. von Arnim, L. Witters, D. Meyer, S. Biesemans, and M. Jurczak, "Multi-gate devices for the 32nm technology node and beyond." in *Proc. 37th European Solid State Device Research Conference ESSDERC 2007*, pp. 143–146, 2007.

[3] J. M. Larson and J. P. Snyder, "Overview and status of metal S/D Schottky-barrier MOSFET technology." *IEEE Trans. Electron Devices*, vol. 53, no. 5, pp. 1048–1058, 2006.

[4] A. Kloes and A. Kostka, "A new analytical method of solving 2D Poisson's equation in MOS devices applied to threshold voltage and subthreshold modeling." *Solid-State Electronics*, vol. 36, no. 12, pp. 1761–1775, 1996.

[5] M. Schwarz, M. Weidemann, A. Kloes, and B. Iñíguez, "2D Analytical Calculation of the Electrostatic Potential in Lightly Doped Schottky barrier Double-Gate MOSFET." *Solid-State Electronics*, vol. Vol. 54, No. 11, pp. 1372–1380, 2010.

[6] M. Schwarz, T. Holtij, A. Kloes, and B. Iñíguez, "2D Analytical Calculation of the Electric Field in Lightly Doped Schottky Barrier Double-Gate MOSFETs and Estimation of the Tunneling/Thermionic Current." *submitted to Solid-State Electronics*, 2011.

[7] G. Wentzel, "Eine Verallgemeinerung der Quantenbedingungen für Würfel Zwecke der Wellenmechanik." *Z. Physik*, vol. 38, pp. 518–529, 1926.

[8] K. K. N. S. M. Sze, *Physics of Semiconductor Devices*. John Wiley & Sons, 2007.

[9] Synopsys, *TCAD Sentaurus*. Synopsys, Inc., c-2009.06 ed., 2009.

Fabrication and characterization of intrinsic WO_3 nanoneedles-based layers deposited onto microhotplates gas sensor substrates via AACVD method

T. Stoycheva*[1], S. Vallejos[2], C. Blackman[2], I. Gràcia[3], X. Correig[1]
[1]Departament d'Enginyeria Electronica, Universitat Rovira i Virgili, Tarragona, Spain
[2]Department of Chemistry, University College London, London, UK
[3]Centro Nacional de Microelectrónica, CNM-CSIC, Bellaterra, Spain

*Toni Stoycheva, Departament d'Enginyeria Electrònica, Electrica i Automàtica, URV
Avinguda dels Paisos Catalans, 26 Campus Sescelades, 43007 TARRAGONA (Spain)
Tel. +34 977 256 571, e-mail: tonistoycheva@yahoo.com

Abstract

Aerosol Assisted Chemical Vapour Deposition (AACVD) was implemented to grow tungsten oxide (WO_3) layers with nanoneedle-like morphology onto microhotplate gas sensor substrates using $W(OPh)_6$ as a precursor. The nanostructured WO_3 sensing layers were growth at three different deposition temperatures – 350ºC, 450ºC and 500ºC. The WO_3 gas sensor deposited at 450ºC and based on nanoneedles showed high selectivity against to NO_2. The sensing properties of WO_3 nanoneedle-like structure, as well as influence of the deposition temperature on their sensing properties were examined in this work.

1. Introduction

Gas sensor based on alumina substrates present disadvantages such as very high power consumption and the non-possibility of the integration of signal-conditioning, signal-processing and control circuitry onto the same substrate. A way to overcome these limitations is using silicon-based micromachined technology to fabricate the gas sensor devices or arrays [1].

In this context, our study deals with the deposition of WO_3 nanostructures by AACVD onto microhotplate gas sensor substrates, where such technique [2] allows a flexible environment and easy implementation for gas sensor fabrication. In this work, we have obtained nanostructured materials at three different deposition temperatures. Moreover, we have studied the influence of deposition temperature on the gas sensing properties of these structures.

2. Experimental details

2.1. Equipment set-up

The AACVD method was implemented for deposition of the gas sensing WO_3 layers. The WO_3 layers were deposited onto microhotplate (MHP) gas sensor substrates, which were designed with low power consumption well-controlled temperature distribution across the sensing layer and high mechanical strength by CNM (National Center of Microelectronics), Barcelona, Spain [3].

Similarly, to our previous study [4] tungsten hexaphenoxide [$W(OPh)_6$] [5] has been used as precursor and dissolved in a mixture of acetone and toluene (50:50, volume), while the molar concentration was kept constant at 0,67 mM. The MHP gas sensor substrate has been placed and heated into the chamber of the custom-made AACVD reactor, where the aerosol was generated ultrasonically. The aerosol of precursor and solvent was then transported by a carrier nitrogen gas onto a heated substrate whit a gas flow rate of 0.5 l/min^{-1}. The nanostructured WO_3 sensing layers were deposited at three different temperatures – 350ºC, 450ºC and 500ºC. Under these conditions the time of the deposition was typically between 30 to 70 min.

2.2. Gas sensing characterization

The three types of MHP WO_3 gas sensors were fabricated and connected to the continuous flow gas test chamber, whit a volume of approximately 280 cm^3. The electrical resistance changes of the WO_3 gas sensors were measured by the computer-controlled characterization system which consists of a custom-made gas sensors test chamber, a gas delivery system and an electrometer from Keathley Instruments Inc. (model 6517A) with a data acquisition card (model 6522). The sensors were exposed to each gas concentration for 10 min after that, air was purged for 20 min. Each measurement was repeated 5 times.

3. Results and discussion

3.1. Films morphology and structural analysis

Scanning electron microscopy was used for detailed analysis of the deposited layers. The result confirmed a presence of a high density, non-aligned nanoneedles in 450ºC/WO_3 and 500ºC/WO_3 samples, while the nanostructure observed at 350ºC/WO_3 sample was similar to nanoparticles with mean diameter of the grains of ~ 300 nm. According to our first study randomly orientated WO_3 nanoneedles were observable at 500ºC or higher deposition temperatures. The ESEM images of the observed WO_3 nanostructures are presented in Fig.1.

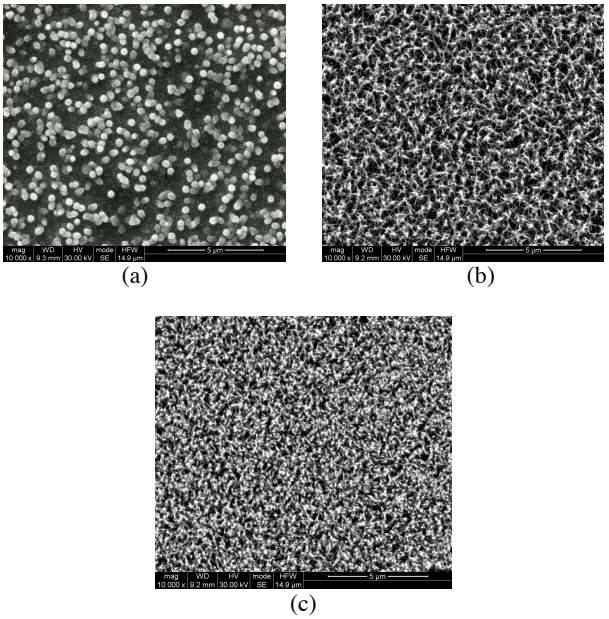

(a) (b) (c)

Fig. 1. Scanning electron microscopy of WO_3 deposited by AACVD onto MHP from reaction of $W(OPh)_6$ in acetone + toluene at 350ºC (a), 450ºC (b) and 500ºC (c)

3.2. Gas sensing properties

The response of the WO_3 to various toxic gases was analyzed at operating temperatures in a range from 100°C to 300°C. The WO_3 gas sensor based on nanoneedles deposited at 450ºC had showed high sensor response (S=22.17) against to NO_2 at lower (100ºC) operating temperatures compared with sensor deposited at 350ºC and 500ºC (fig.2). Moreover, the MHP 450ºC/WO3 nanoneedles gas sensors had shown better response and recovery times even at this operating temperature, comparing with the alumina WO_3 nanoneedles gas sensors. Furthermore, the response to other contaminants such as H_2S, CO and C_6H_6 was detected, at relatively low (150ºC) operating temperature. Such behavior was not observable in our previous study [4] for sensor deposited onto alumina gas sensor substrate. Target gases, their concentrations and some of the obtained results in the experiments are presented in Fig.3. In the case of oxidizing gas the response was calculated as S = Rgas/Rair and for reducing gas S = Rair/Rgas.

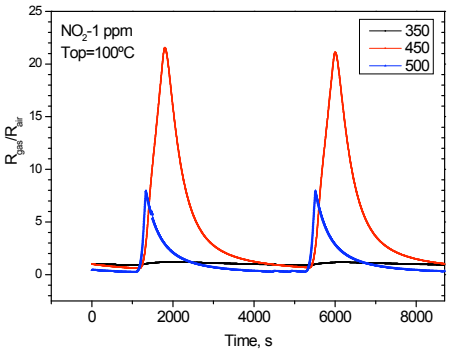

Fig. 2. Response of intrinsic WO_3 nanoneedles based gas sensors to NO_2.

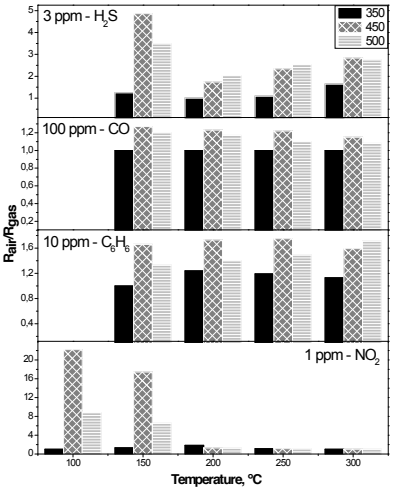

Fig.3. Sensor responses to various gaseous species and operating temperatures

3. Conclusions

Gas sensors based on nanostructured WO_3 were fabricated by AACVD onto MHP gas sensor substrates. The sensing properties of these structures to various contaminant species were studied. The gas sensing characterization revealed a high selectivity of WO_3 morphologies to NO_2. The WO_3 nanowires based sensors have a lower optimun operating temperature at 150ºC or below. The gas sensor based on WO_3 nanoneedle-like layers deposited at 450ºC deposition temperature result in better response than gas sensor deposited at 350ºC and 500ºC.

References

[1] A. Götz, *et al.*, "A novel methodology for the manufacturability of robust CMOS semiconductor gas sensor arrays," *Sensors and Actuators, B: Chemical*, vol. 77, pp. 395-400, 2001.

[2] X. H. Hou and K. L. Choy, "Processing and applications of aerosol-assisted chemical vapor deposition," *Chemical Vapor Deposition*, vol. 12, pp. 583-596, 2006.

[3] R. Inglés, *et al.*, "Electro-thermal simulation and characterization of preconcentration membranes," *Sensors and Actuators A: Physical*, vol. In Press, Corrected Proof.

[4] T. Stoycheva, *et al.*, "Characterization and gas sesing properties of intrinsic and Au-doped WO3 nanostuctures deposited by AACVD technique," *Procedia Engineering*, vol. 5, pp. 131-134, 2010.

[5] W. B. Cross, *et al.*, "Tungsten Oxide Coatings from the Aerosol-Assisted Chemical Vapor Deposition of W(OAr)6 (Ar = C6H5, C6H4F-4, C6H3F2-3,4); Photocatalytically Active γ-WO3 Films," *Chemistry of Materials*, vol. 15, pp. 2786-2796, 2003.

Anodized based MOX nanostructured materials for gas sensor application

R. Vázquez, R. Calavia, E. Llobet

MINOS-EMaS, Universitat Rovira i Virgili, 43006 Tarragona, Spain
raul.calavia@urv.cat
eduard.llobet@urv.cat
rosamaria.vazquez@estudiants.urv.cat

Abstract

In this paper we want to present two methods to obtain nanostructured materials for gas sensing application. These methods are based in anodic oxidation of aluminum. Morphological characterization was carried out in both cases. MOX nanostructured materials with high surface/volume ratio had been obtained by anodic oxidation.

1. Introduction

Interest in nanostructured metal oxides for gas sensing application has been increasing in last years [1]. This type of material is very attractive because its area/volume ratio increases the sensitivity [2], so these nanostructured materials are very promising for gas sensor application.

In this work we want to show two approaches to obtain nanostructured materials via anodic oxidation that will be characterized as a gas sensor.

First approach consists in to fabricate porous alumina and then to cover with a sensitive material (fig. 1). In past works we used sputtering technique to cover the nanostructured [3]. The novelty in this work is the use of the ALD technique, which it allows to conformally deposit layers with a thickness between 10 and 1 nm.

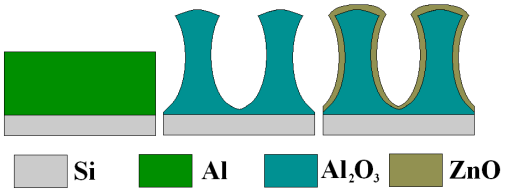

Fig.1. Schematic nanoporous alumina covered ZnO

The second approach consists in to obtain TiO_2 nanocolumns through anodization of aluminium (fig.2).

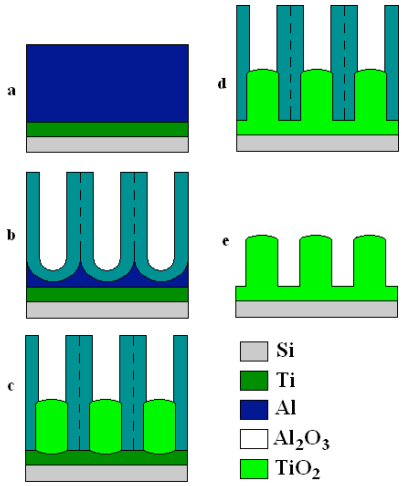

Fig.2. Schematic to obtain TiO_2 nanocolumns

2. Experimental

Here we present the experimental procedure used at the two approaches. In both cases a Si wafer with 2" of diameter was employed as a substrate.

- First approach: nanoporous alumina covered with ZnO using ALD technique

The structure of samples is composed by the following layers: 20 nm titanium adhesive layer and 600 nm of aluminium layer deposited onto the substrate using sputtering process. Wafers were cut in four pieces. These pieces were introduced individually into a two electrode cell made of teflon which allows to obtain 1.5 cm^2 anodised area. For the anodising process, the electrolyte employed was 0.4 M tartaric acid, and used control current mode in the pores formation process fixed at 5.33 mA/cm^2 and maximum voltage at 350 V. Some samples were pore widened with 5%wt H_3PO_4 (phosphoric acid) during 10 min. Finally, samples were covered with ZnO using ALD deposition technique. The estimated thickness was 10 nm, 5 nm and 1 nm.

- Second approach: TiO_2 nanocolumms obtained through aluminium anodization

In this case the structure of samples were as follows: it was used 300 nm thick titanium layer, which will be used for growing TiO_2 nanocolumns, and 600 nm thick aluminium layer, through which they were anodised titanium. In the same way that in the first approach, samples were cut in four pieces, and anodised individually. In this case we used two step anodising process. First, we anodised using current control at 5.33 mA/cm^2 for 120 V with 0.4 M malonic acid. Then the electrolyte was switched to 0.4 M tartaric acid and the voltage has been increased to 350 V (fig. 3).

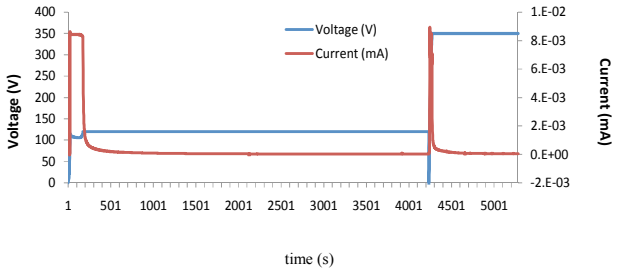

Fig. 3. I-V characteristic for two anodising process

3. Results

For samples obtained with both methods has been done morphological characterization.

In the first method we estimated by FIB-ESEM that the growth of ZnO layer deposited onto nanoporous alumina is about 12 nm, and it was obtained conformal coating of material.

For the second method, Figure 4 shows ESEM images of TiO_2 obtained by anodic oxidation.

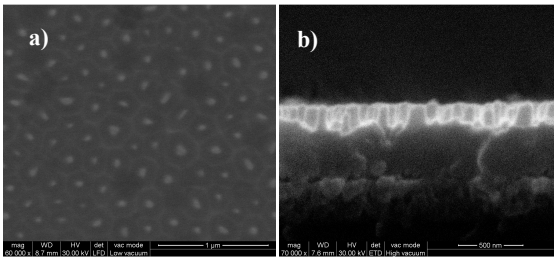

Fig. 4. ESEM imagesTiO_2 nanocolumns

In this case, we estimated a diameter of nanocolumns of about 85 nm and a high of 170 nm. The structure of nanocolumns obtained is semi-ordered.

4. Conclusions and future work

We have obtained nanostructured materials using two different methods based on aluminium anodization.

For the first method it was obtained thin layer of ZnO (12 nm) deposition.

We have been obtained TiO_2 nanostructure with a great length/diameter aspect ratio.

These results are very promising for gas sensor due to the high surface/volume ratio obtained.

In the near future we will characterize these materials for gas sensor application.

References

[1] G. Jiménez-Cadena, J. Riu and F. X. Rius, "Gas sensors based on nanostructured materials", Analyst, 2007, 132, 1083-1099.

[2] Isolde Simon, Nicolae Bârsan, Michael Bauer and Udo Weimar, "Micromachined metal oxide gas sensors: opportunities to improve sensor performance

[3] R. Calavia, A. Mozalev, R. Vazquez, I. Gracia, C. Cané, X. Vilanova, X. Correig and E. Llobet, "Porous alumina covered by WO_3 sputtered layer as sensing material for MEM gas sensor", Proceedings Ibernam 2009.